

The XMAGNET exascale MHD simulations of SMBH feedback in galaxy groups and clusters: Overview and preliminary cluster results

PHILIPP GRETE ¹, BRIAN W. O’SHEA ^{2,3,4,5}, FORREST W. GLINES ⁶, DEOVRAT PRASAD ⁷,
BENJAMIN D. WIBKING ³, MARTIN FOURNIER ¹, MARCUS BRÜGGEN ¹ AND MARK VOIT ³

¹University of Hamburg, Hamburger Sternwarte, Gojenbergsweg 112, 21029 Hamburg, Germany

²Department of Computational Mathematics, Science, & Engineering, Michigan State University, 428 S. Shaw Lane, East Lansing, MI 48824

³Department of Physics & Astronomy, 567 Wilson Road, Michigan State University, East Lansing, MI 48824

⁴Facility for Rare Isotope Beams, Michigan State University, 640 S. Shaw Lane, East Lansing, MI 48824

⁵Institute for Cyber-Enabled Research, 567 Wilson Road, Michigan State University, East Lansing, MI 48824

⁶Theoretical Division, TA-3 Bldg. 123, Los Alamos National Laboratory, Los Alamos, NM 87545

⁷School of Physics and Astronomy, Cardiff University, 5 The Parade, Cardiff CF24 3AA, UK

ABSTRACT

We present initial results from extremely well-resolved 3D magnetohydrodynamical simulations of idealized galaxy clusters, conducted using the AthenaPK code on the Frontier exascale supercomputer. These simulations explore the self-regulation of galaxy groups and cool-core clusters by cold gas-triggered active galactic nucleus (AGN) feedback incorporating magnetized kinetic jets. Our simulation campaign includes simulations of galaxy groups and clusters with a range of masses and intragroup and intracluster medium properties. In this paper we present results that focus on a Perseus-like cluster. We find that the simulated clusters are self-regulating, with the cluster cores staying at a roughly constant thermodynamic state and AGN jet power staying at physically reasonable values ($\simeq 10^{44} - 10^{45}$ erg/s) for billions of years without a discernible duty cycle. These simulations also produce significant amounts of cold gas, with calculations having strong magnetic fields generally both promoting cold gas formation and allowing cold gas out to much larger clustercentric radii ($\simeq 100$ kpc) than simulations with weak or no fields ($\simeq 10$ kpc), and also having more filamentary cold gas morphology. We find that AGN feedback significantly increases the strength of magnetic fields at the center of the cluster. We also find that the magnetized turbulence generated by the AGN results in turbulence where the velocity power spectra are tied to AGN activity whereas the magnetic energy spectra are much less impacted after reaching a stationary state.

Keywords: Galaxy clusters (584), Galaxy Jets (601), Intracluster medium (858), Magnetic fields (994)

1. INTRODUCTION

The intracluster medium (ICM) – the hot, diffuse, magnetized plasma that comprises the bulk of the baryons in galaxy clusters – radiates copiously in X-ray radiation, with X-ray luminosities of massive clusters typically being in the range of $\sim 10^{43.5} - 10^{45.5}$ erg/s (Fabian 1994). “Cool core” galaxy clusters, having dense and (relatively) cool cores, are particularly X-ray luminous, with central cooling times of tens to hundreds of millions of years – far shorter than the age of the universe and the lifetime of these structures. (Hudson et al. 2010)

In cool-core clusters, local thermal stability of the intracluster medium becomes a critical physical phenomenon that governs their evolution (Field 1965). Cold gas is expected to precipitate out of the thermally unstable ICM (Voit et al. 2008; McCourt et al. 2012) and to be available to star formation and accretion onto the central SMBH (Oosterloo et al. 2024; Guo et al. 2024). An apparent consequence is that this rapidly cooling gas should result in many hundreds to thousands of Solar masses per year of cold, dense gas being available for star formation, and thus that the brightest central galaxies in clusters should see similarly high star formation rates. However, the observed star formation rate

in these galaxies is lower – typically only a handful of solar masses per year (Fabian et al. 1984; Edge 2001; Peterson et al. 2003; O’Dea et al. 2008).

This observation implies that there is a heating source in the center of every cool-core galaxy cluster that offsets this cooling, and does so in a tightly-coupled way that inhibits significant amounts of gas from forming (Pizzolato & Soker 2005). While many mechanisms have been proposed, including thermal conduction, supernova feedback, sound waves, and cluster mergers, the only mechanism that robustly fits the necessary criteria of (1) appropriate level of energy production, (2) location that would tend to deposit heat in the areas of greatest X-ray emission/cooling, and (3) ability to couple to the central cluster plasma on short time scales, is AGN feedback (Churazov et al. 2001; Bîrzan et al. 2004; Rafferty et al. 2006, 2008; Cavagnolo et al. 2008, 2010; Sun et al. 2009). This idea has been supported by observational evidence from radio surveys showing that radio-loud AGN at the centers of massive cool-core galaxies are always active and, separately, analysis of cavities created by AGN jets interacting with the ICM demonstrates that the work done by those “bubbles” over time is roughly what is needed to offset cooling in clusters (e.g., Bîrzan et al. 2004; Panagoulia et al. 2014; Prunier et al. 2024).

These observations are supported by theory and simulations that have shown AGN feedback is crucial to the self-regulation of clusters (e.g., Gaspari et al. 2012, 2013; Li et al. 2015; Prasad et al. 2015; Voit et al. 2017; Meece et al. 2017; Donahue & Voit 2022; Nobels et al. 2022; Ehlert et al. 2023). Idealized simulations of AGN feedback in galaxy clusters have demonstrated that cold gas-triggered AGN hosted by the central cluster galaxy are effective mechanisms for offsetting radiative losses in the intracluster medium, and (depending on the exact prescription for AGN triggering and feedback) result in clusters with thermodynamic states that are comparable to observed cool-core clusters (e.g., Li & Bryan 2014; Qiu et al. 2019; Beckmann et al. 2019; Wang et al. 2021; Ehlert et al. 2023; Fournier et al. 2024). Furthermore, theory has shown that AGN feedback is important in environments less extreme than galaxy clusters. Cosmological simulations of galaxy formation show that AGN feedback is necessary to correctly reproduce the low star formation rates in massive galaxies (e.g., Naab & Ostriker 2017; Donahue & Voit 2022) as well as the budget of cold-phase gas (e.g., Olivares et al. 2019). It is challenging to make detailed inferences from these simulations, however, because implementations of AGN feedback operate at the resolution limit of these calculations (i.e., on \sim kpc scales) and thus cannot accurately cap-

ture the interaction between the jet and the cooling, multi-phase gas. In addition, these simulations do not reproduce the morphology of the radio jets that dominate the radio sky (e.g., Shimwell et al. 2022).

It is clear that there is need for a detailed examination of the impact of AGN feedback in self-regulating cool-core clusters. Multi-wavelength observations of these systems have recently shed light on the multiphase nature of the intracluster medium, showing significant complexity at relatively small spatial scales (e.g., Salomé et al. 2006; McNamara et al. 2014; Tremblay et al. 2018; Olivares et al. 2019; Vantyghem et al. 2021; Gingras et al. 2024). Filament-like structures of magnetically-supported warm ionized and cold molecular gas are expected to populate the inner tens of kpc of potentially all cool-core clusters (Olivares et al. 2019). The measured velocity structure functions and X-ray surface brightness fluctuations also imply that the ICM is turbulent, although this turbulence is subsonic (Li et al. 2020; Ganguly et al. 2023; de Vries et al. 2023).

While subsonic (and thus subdominant in terms of the system’s overall pressure support), this turbulence may be quite important for promoting thermal instability and energy transfer. Highly idealized simulations using Cartesian, turbulent boxes have shown that the formation of cold structures and the coupling between gas phases is tightly coupled to turbulence driving, magnetic fields, and potentially other physical processes (McCourt et al. 2012; Gaspari et al. 2013; Ji et al. 2018; Mohapatra et al. 2022, 2023; Wibking et al. 2024). While these setups are useful for parametric studies and provide a way to probe the effects of turbulence in hot plasmas, they rely on simplified models of turbulence driving, missing the anisotropic and intermittent nature of AGN feedback as well as the impact of the overall cluster environment.

In this paper we present the first results from the XMAGNET (“eXascale simulations of Magnetized AGN feedback focusing on Energetics and Turbulence”) project¹ – a suite of very high resolution 3D magnetohydrodynamical simulations of idealized galaxy groups and clusters that were run on Frontier², the first exascale supercomputer available to academic researchers (Atchley et al. 2023). These simulations, run using the AthenaPK code, include gravity, radiative cooling, and a model of

¹ See <https://xmagnet-simulations.github.io> for further material including videos.

² Frontier is operated by the Oak Ridge National Laboratory’s Leadership Computing Facility on behalf of the Department of Energy. This work is supported by the DOE INCITE program under allocation AST-146 (2023-2024).

cold gas-triggered AGN feedback that converts accreted gas into bipolar magnetized kinetic jets and thermal energy. The goal of this simulation suite is to understand, using extremely large dynamic range and physics-rich calculations with very well-resolved core regions, the accretion of gas onto supermassive black holes, the impact of the resulting magnetized AGN jets on the circumgalactic and intracluster plasma. By resolving the inner regions of these idealised systems with extremely large uniform-resolution grids, we attempt to bridge the gap between realistic but relatively poorly resolved cosmological simulations of groups and galaxies (e.g., Pellissier et al. 2023; Schaye et al. 2023; Nelson et al. 2024) and high-resolution but also highly idealized turbulent boxes (Grete et al. 2021, 2023; Federrath et al. 2021; Beattie et al. 2024). This use of large, fixed central grids allows us to quantitatively study the evolution of the intracluster and intragroup medium with no artifacts resulting from changes in refinement. In particular, we wish to examine the interactions between the AGN jets and their environments, including the driving of turbulence and dissipation of energy, the amplification and structure of magnetic fields in groups and clusters, and the impact that these phenomena have on the formation of cold, dense gas that may, in turn, feed the supermassive black hole and power the AGN.

In this paper we focus on a subset of our calculations – a suite of idealized galaxy clusters with masses and other properties comparable to the Perseus cool-core cluster, with AGN feedback triggered by the formation of cool gas in the vicinity of the central supermassive black hole – and present key results from those calculations. Following papers will delve deeper into the evolution of magnetized turbulence in these clusters, closer comparisons to observation, the formation and properties of cold, magnetized filaments in the center of the clusters, and of halos with a range of different virial masses and properties.

This paper is structured as follows: In Section 2 we describe our code and numerical methods, simulation setup, and the details of our AGN triggering and feedback algorithms. In Section 3 we survey the key results from the simulation suite, and discuss those results in Section 4. Finally, in Section 5 we summarize our results and discuss future work that will emerge from analysis of this simulation suite.

2. METHODS

In this section, we describe the ATHENAPK code (Section 2.1), the numerical methods that we use for these simulations, including the prescription used for AGN

triggering and feedback (Section 2.2), and summarize the entire simulation suite (Section 2.3).

2.1. The ATHENAPK code

ATHENAPK is an open source, performance portable, finite volume (magneto)hydrodynamics code based on the adaptive mesh refinement framework PARTHENON (Grete et al. 2023) – originally derived from ATHENA++ (Stone et al. 2020). Performance portability refers to the capability to compile (and optimize) the code to various architectures (such as CPUs with different architecture or GPUs from different vendors) using a single code base and is realized by use of the KOKKOS programming model (Trott et al. 2022). ATHENAPK has proven scalability to the largest scales possible today, e.g., $\gtrsim 93\%$ weak scaling up to 73,000 GPUs on Frontier (TOP500 #1 from 06/2022 to 06/2024). Further details on the challenges encountered running large scale simulation are detailed in Sec. 4.5.

While ATHENAPK implements a variety of numerical methods, all simulations presented in this paper employ an overall second-order accurate, shock-capturing, finite volume scheme consisting of RK2 time integration, piecewise-linear reconstruction, and a HLLD (MHD) or HLLC (hydro) Riemann solver (Miyoshi & Kusano 2005). The resulting mass fluxes calculated from the Riemann solver are also used to advect an arbitrary number of passive tracer fluids. In the MHD case, the hyperbolic divergence cleaning method presented in Dedner et al. (2002) handles the $\nabla \cdot \mathbf{B} = 0$ constraint. Optically thin cooling is calculated by the extract integration method introduced by Townsend (2009).

For numerical stability – especially in cases where the fast, hot jet interacts with cold clumps, first order flux correction is used. All fluxes in cells for which a normal update would yield a negative pressure or density are recalculated using a more diffusive scheme consisting of piecewise constant reconstruction and an LLF Riemann solver.

Simulations were conducted using commit 3ce0a88 and the complete input file for the Fiducial simulation is available online as supplemental material.

2.2. Simulation Setup

The simulations are run on a Cartesian grid in a cubic volume with a side length of 6.4 Mpc, covered by $1,024^3$ cells in the base grid in a hierarchy of static meshes. We enforce 3 levels of refinement with $[-400, 400]^3$ kpc (where the root grid is the 0th level), 5 levels of refinement on $[-200, 200]^3$ kpc, and 6 levels of refinement on $[-125, 125]^3$ kpc. Thus, the central region of the simulation is covered with a uniform grid of $2,560^3$ cells with cell side length of $\Delta_x \approx 100$ pc.

Cosmological expansion is neglected in these simulations. We used a vanilla Λ CDM model to get the virial mass of the NFW halo and to set its gas temperature. We set redshift $z = 0$ at initialization with $\Omega_M = 0.3$, $\Omega_\Lambda = 0.7$, and $H_0 = 70 \text{ km s}^{-1}$. We note that the precise details of the cosmological model do not impact the results presented in later sections of this paper, which pertain to baryonic physics in the halo core.

The specific values given along the individual method descriptions pertain to the Perseus-like cluster setup.

2.2.1. Gravitational Potential

The gravitational potential has three components: a dark matter halo profile, a BCG with a mass profile, and a SMBH. The dark matter follows the NFW profile (Navarro et al. 1997), using $M_{\text{NFW}} = 6.6 \times 10^{14} M_\odot$ for the mass of the halo (corresponding to M_{200} , i.e., the mass contained within the virial radius r_{200} within which the mean enclosed mass density is 200 times the critical density of the Universe at the cluster redshift; Simionescu et al. 2011) and a concentration parameter $c_{\text{NFW}} = 6$. The gravitational field from the NFW profile takes the form

$$g_{\text{NFW}}(r) = \frac{G M_{\text{NFW}}}{r^2} \frac{\left[\ln \left(1 + \frac{r}{R_{\text{NFW}}} \right) - \frac{r}{r + R_{\text{NFW}}} \right]}{\ln(1 + c_{\text{NFW}}) - \frac{c_{\text{NFW}}}{1 + c_{\text{NFW}}}}. \quad (1)$$

The scale radius, R_{NFW} , for the NFW profile is computed from

$$R_{\text{NFW}} = \left(\frac{M_{\text{NFW}}}{4\pi\rho_{\text{NFW}} \left[\ln(1 + c_{\text{NFW}}) - \frac{c_{\text{NFW}}}{1 + c_{\text{NFW}}} \right]} \right)^{1/3}, \quad (2)$$

where the scale density ρ_{NFW} is computed from

$$\rho_{\text{NFW}} = \frac{200}{3} \rho_{\text{crit}} \frac{c_{\text{NFW}}^3}{\ln(1 + c_{\text{NFW}}) - c_{\text{NFW}}/(1 + c_{\text{NFW}})}. \quad (3)$$

The critical density, ρ_{crit} , is defined as:

$$\rho_{\text{crit}} = \frac{3H_0^2}{8\pi G}. \quad (4)$$

We use a Hernquist BCG profile

$$g_{\text{BCG}}(r) = G \frac{M_{\text{BCG}}}{R^2} \frac{1}{\left(1 + \frac{r}{R}\right)^2} \quad (5)$$

with $M_{\text{BCG}} = 2.4 \times 10^{11} M_\odot$ and $R_{\text{BCG}} = 10 \text{ kpc}$ (Mathews et al. 2006).

We include the gravitational field from a SMBH black hole with $M_{\text{SMBH}} = 1.1 \times 10^9 M_\odot$ at the center of the cluster halo (Riffel et al. 2020), which is coincident with the center of both the dark matter and BCG halos.

2.2.2. Entropy Profile

We initialize the specific entropy as a function of radius, where entropy K is defined as

$$K \equiv \frac{k_b T}{n_e^{2/3}} \quad (6)$$

where k_b is Boltzmann's constant, T is the temperature, and n_e is the electron density. We set the initial entropy profile of the gas as a power law plus a constant floor using the same form as the ACCEPT database (Cavagnolo et al. 2009)

$$K(r) = K_0 + K_{100} (r/100 \text{ kpc})^{\alpha_K}, \quad (7)$$

where $K(r)$ is the specific entropy as a function of radius and K_0 , K_{100} , and α_K are parameters. We use $K_0 = 20.0 \text{ keV cm}^2$, $K_{100} = 110.0 \text{ keV cm}^2$, and $\alpha_K = 1.1$ for the initial entropy profile of a Perseus-like cluster.

2.2.3. Initial Pressure and Density (Hydrostatic Equilibrium)

We compute the initial pressure and density by enforcing the initial cluster to be in hydrostatic equilibrium given the gravitational profile described above and the ACCEPT-like entropy profile, assuming an ideal gas with adiabatic index $\gamma = 5/3$. In order to close the set of equations to define the initial gas profile, we fix the gas density at $r = 1.8 \text{ Mpc}$ to $\rho = 9.47 \times 10^{-29} \text{ g cm}^{-3}$.

2.2.4. Initial velocity and magnetic field perturbations

In order to break symmetry in the initial conditions and seed a weakly turbulent background state, we initialize both the velocity and magnetic field with perturbations. They are generated in spectral space, each based on 40 wavemodes chosen randomly within an interval of characteristic scales between 50 and 200 kpc. The amplitudes are set by an inverse parabolic shape with a peak at a characteristic lengthscale of 100 kpc and scaled to to a root mean squared velocity of 75 km/s and magnetic field of $1 \mu\text{G}$.

2.2.5. Cooling and plasma composition

We use a helium mass fraction $\chi = 0.25$, with the remaining baryonic mass being hydrogen and electrons, which allows temperature T to be defined from density ρ and pressure P following

$$T = \frac{\mu m_h P}{k_B \rho}. \quad (8)$$

where m_h is the atomic mass of hydrogen, k_B is Boltzmann's constant, and μ is the mean particle mass per m_h , found by

$$\mu = \left[\frac{3}{4}\chi + 2(1 - \chi) \right]^{-1}. \quad (9)$$

The plasma cooling rate (i.e., radiative loss rate) is based on tabulated tables from Schure et al. (2009) assuming $1 Z_{\odot}$ metallicity for all our runs except for our “weak cooling” simulation where we assume a metallicity of $0.3 Z_{\odot}$. While most previous work assumes one-third Solar metallicity for their fiducial run (e.g., Li & Bryan 2014; Wang et al. 2021), observations of cool-core clusters conclude that the metallicity of the ICM in the core region is usually closer to $0.5 - 1 Z_{\odot}$, and decreases with increasing radius to reach roughly one-third Solar metallicity for $r \sim 100$ kpc (Sanders & Fabian 2007; McDonald et al. 2019). It is thus likely that our strong cooling simulations overestimate cooling for radii larger than a few tens of kpc, and that our weak cooling simulation underestimates cooling in the core region.

2.2.6. AGN Feedback

We include AGN feedback using thermal heating, kinetic jet, and magnetic tower models exploring different relative strengths. We divide the AGN feedback between the three channels following

$$\dot{E}_{\text{AGN}} = \dot{E}_T + \dot{E}_K + \dot{E}_B = (f_T + f_K + f_B) \dot{E}_{\text{AGN}}. \quad (10)$$

where \dot{E}_{AGN} is the total AGN feedback rate; \dot{E}_T , \dot{E}_K , and \dot{E}_B are the total thermal, kinetic, and magnetic AGN feedback rates; and f_T , f_K , and f_B are the thermal, kinetic, and magnetic fractions of the total AGN feedback rate. Given the scales in our simulations we set $f_T = 0.25$, $f_K = 0.74$ and $f_B = 0.01$ (or $f_K = 0.75$ and $f_B = 0$ in the hydrodynamic case).

A sketch of some of the key model parameters and their values used for the simulations is shown in Fig. 1.

2.2.7. Thermal AGN Feedback

In the thermal feedback model, thermal energy is deposited volumetrically within a sphere around the center of the halo where the presumed AGN resides.

$$\dot{e}_T(r) = \begin{cases} \frac{f_T \dot{E}_{\text{AGN}}}{(4/3)\pi R_T^3}, & \text{if } r \leq R_T, \\ 0, & \text{otherwise,} \end{cases} \quad (11)$$

where we use $R_T = 1$ kpc for the radius of thermal feedback. We also inject mass proportional to the thermal feedback at uniform density throughout the sphere of thermal injection

$$\dot{\rho}_T(r) = \begin{cases} \frac{f_T \dot{M}_{\text{AGN}}}{\frac{4}{3}\pi R_T^3}, & \text{if } r \leq R_T, \\ 0, & \text{otherwise,} \end{cases} \quad (12)$$

so that the total mass injected will match

$$\dot{M}_T = f_T \dot{M}_{\text{AGN}}. \quad (13)$$

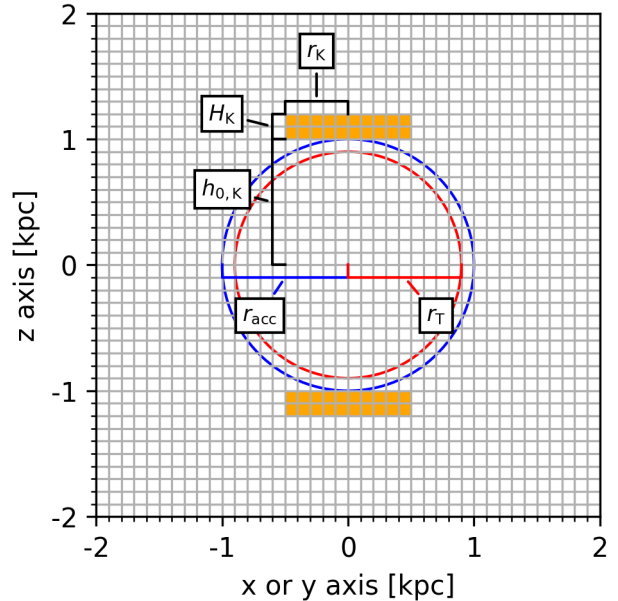


Figure 1. Sketch of some of the key model parameters and their values given the mesh setup in our simulations: the accretion radius, r_{acc} , the thermal feedback radius, r_T (set to a smaller value here for illustrative purposes whereas in the simulations $r_T = r_{\text{acc}}$), the kinetic jet launching radius r_K , height $h_{0,K}$, and offset h_K . Small squares correspond to a single cell in the simulation.

2.2.8. Kinetic AGN Feedback

In the kinetic feedback model, kinetic energy and mass is injected into two disks offset above and below the midplane of the AGN jet. These disks have a radius of R_K , each with thickness H_K , and are offset from the midplane by $h_{0,K}$ such that kinetic feedback is injected as far away from the midplane as $H_K + h_{0,K}$. The rate of mass-energy injected by the jet is set proportional the fraction of accreted mass afforded to kinetic feedback, with ϵ fraction of that mass-energy proportioned to energy, i.e.,

$$f_K \dot{M}_{\text{acc}} c^2 = \dot{M}_K c^2 + \dot{E}_K \quad (14)$$

$$\dot{M}_K = (1 - \epsilon) \dot{M}_{\text{acc}} \quad (15)$$

$$\dot{E}_K = \epsilon \dot{M}_{\text{acc}} c^2, \quad (16)$$

$$(17)$$

where c is the speed of light. The jet then injects a mass density

$$\dot{\rho}_K = \frac{\dot{M}_K}{2\pi R_K^2 H_K}, \quad (18)$$

where $R_K = 500$ pc and $H_K = 2\Delta_x \approx 200$ pc. The jet speed of the injected material is given by:

$$v_K = \sqrt{2(\eta c^2 - (1 - \eta) u_{\text{jet}})}, \quad (19)$$

where $\eta = 10^{-3}$ is the feedback power efficiency and u_{jet} the specific internal energy of the jet (here set by a temperature $T_{\text{jet}} = 10^8$ K). The momentum of the injected material is aligned with the z -axis of the Cartesian coordinate system.³ The momentum density injected is then given by:

$$\dot{\mathbf{M}}_K(\mathbf{r}) = \begin{cases} \text{sign}(z)\dot{\rho}_K v_K \hat{h}, & \text{if } r \leq R_K \text{ and } h_{0,K} \leq |h| \leq h_{0,K} + H_K \\ 0, & \text{otherwise,} \end{cases} \quad (20)$$

where r here is the distance from the jet axis and h is the signed height above or below the mid plane. The injected kinetic energy rate per volume is

$$\dot{\mathbf{e}}_K(\mathbf{r}) = \begin{cases} \frac{1}{2}\dot{\rho}_K v_K^2, & \text{if } r \leq R_K \text{ and } |z| \leq H_K, \\ 0, & \text{otherwise,} \end{cases} \quad (21)$$

so that the total kinetic energy injected matches $f_K E_{\text{AGN}}$.

2.2.9. Magnetic AGN Feedback

In general, the magnetic AGN feedback implementation consists of two key pieces: the magnetic field configuration and its normalization to match the target power.

For the magnetic field configuration, we use a simple closed field loop model – effectively a magnetic donut – given by the following vector potential

$$A_h(r, \theta, h) = \begin{cases} B_0 L_M \exp(-r^2/L_M^2), & \text{if } h_{0,M} \leq |h| \leq h_{0,M} + h_M, \\ 0, & \text{otherwise,} \end{cases} \quad (22)$$

where B_0 is a to be determined normalization factor, L_M a characteristic length scale, and $h_{0,M}$ and h_M the injection offset in vertical direction and injection height, following the kinetic parameters. Using the vector potential as basis allows the resulting magnetic field

$$B_\theta(r, \theta, h) = \begin{cases} 2B_0 r/L_M \exp(-r^2/L_M^2), & \text{if } h_{0,M} \leq |h| \leq h_M + h_{0,M} \\ 0, & \text{otherwise.} \end{cases} \quad (23)$$

to be divergence-free to machine precision. For all simulations the scales are chosen⁴ such that the magnetic

donut is effectively seeded within the kinetic jet launching region, i.e., $h_{0,M} = h_{0,K} = 1$ kpc, $h_M = h_K = 2\Delta_x \approx 200$ pc, and $L_M = 250$ pc.

Given that the injected magnetic field strength should be normalized with respect to a target power rather than a fixed strength we apply the following steps:

To inject a magnetic field of strength B_0 , we set the initial magnetic field to $\mathbf{B} = \mathcal{B}|_{\mathcal{B}_0=B_0}$ with the vector field \mathcal{B} corresponding to the magnetic field configuration. To inject a field with a rate \dot{B}_0 , we add a magnetic field $\dot{\mathbf{B}} = \mathcal{B}|_{\mathcal{B}_0=\dot{B}_0}$ to the existing fields. Injecting by magnetic power, however, requires extra steps since the increase in magnetic energy depends on the existing magnetic field. Given an existing magnetic field \mathbf{B}_n , injecting a magnetic field of strength B_p (which we need to solve for) leads to a new magnetic field strength

$$\mathbf{B}_{n+1} = \mathbf{B}_n + \mathcal{B}|_{\mathcal{B}_0=B_p}. \quad (24)$$

The change in total magnetic energy is then

$$\Delta E_B = B_p \int_{\Omega} \mathbf{B}_n \cdot \mathcal{B}|_{\mathcal{B}_0=1} dV \quad (25)$$

$$+ B_p^2 \int_{\Omega} \frac{1}{2} \mathcal{B}|_{\mathcal{B}_0=1} \cdot \mathcal{B}|_{\mathcal{B}_0=1} dV, \quad (26)$$

where Ω is the simulation domain. To determine the factor B_p to give the correct increase in magnetic energy, the two integrals in Eq. 25 corresponding to the linear and quadratic contributions must first be computed (via reduction over the entire domain). Then B_p can be determined by the quadratic formula where only one root will be positive. For the case of magnetic field injection by the AGN, the change in magnetic energy is set to $\Delta E_B = \Delta t f_B \dot{E}_{\text{AGN}}$ and B_p is determined by the reductions above.

2.2.10. AGN cold mass triggering

In our simulations, AGN feedback is triggered by cold mass around the presumed AGN. AGN triggering occurs within a $r_{\text{acc}} = 1$ kpc radius accretion zone around the presumed AGN. Within the accretion zone, gas with a temperature below the threshold $T_{\text{cold}} = 5 \times 10^4$ K triggers AGN feedback. The mass accretion rate onto the AGN follows

$$\dot{M}_{\text{AGN}} = \int_{r < r_{\text{acc}}} \rho_{\text{cold}}(\mathbf{r})/t_{\text{acc}} dV, \quad (27)$$

where $\rho_{\text{cold}}(\mathbf{r})$ is equal to $\rho(\mathbf{r})$ in cells where $T(\mathbf{r}) \leq T_{\text{cold}}$ and 0 otherwise, and $t_{\text{acc}} = 100$ Myr is the accretion time scale. The total AGN feedback rate is then set to

$$\dot{E}_{\text{AGN}} = \epsilon_{\text{AGN}} \dot{M}_{\text{AGN}} c^2, \quad (28)$$

³ The implementation of the kinetic feedback model also supports precessing jets, which have not been used in the simulations presented in this paper.

⁴ A more complex pinching magnetic tower model, as well as mass injection associated with the magnetic feedback channel, are also implemented in the code but not used in the simulations presented in this paper given their large-scale focus.

where $\epsilon_{\text{AGN}} = 10^{-3}$ is the efficiency with which rest-mass from the accreted cold gas is turned into feedback energy.

The accreted mass is removed from the simulation. Mass is only removed from cells within the accretion zone if they have a temperature below the cold gas temperature threshold. The density removed follows the rate

$$\dot{\rho}(\mathbf{r}) = \begin{cases} \rho(\mathbf{r})/t_{\text{acc}}, & \text{if } T(\mathbf{r}) < T_{\text{cold}}, \\ 0, & \text{otherwise.} \end{cases} \quad (29)$$

For model completeness we implemented other types of accretion, e.g., “boosted Bondi,” but these are not used in the present simulations.

2.2.11. Stellar feedback

Heat and mass feedback from Type Ia supernovae (SNIa) are injected in a spherically symmetric kernel proportional to the (fixed) stellar mass density of the central cluster galaxy. The energy density and mass density injected into a cell at distance r from the cluster center is

$$\dot{\epsilon}_{\text{SNIa}} = \Gamma_{\text{SNIa}} E_{\text{SNIa}} \rho_{\text{BCG}}(r) \quad (30)$$

$$\dot{\rho}_{\text{SNIa}} = \alpha \rho_{\text{BCG}}(r), \quad (31)$$

where $\Gamma_{\text{SNIa}} = 3 \times 10^{-14} \text{ SNIa yr}^{-1} \text{ Msun}^{-1}$ is the SNIa rate, $E_{\text{SNIa}} = 10^{51} \text{ erg SNIa}^{-1}$ is the energy injected per SNIa, and $\alpha = 10^{-19} \text{ s}^{-1}$ is the mass injection rate by SNIa.

In addition to the SNIa channel we also include a second, instantaneous stellar feedback channel to account for the absence of separate star particles in the simulation. They are typically included as mediators to convert high density gas that would end up in stars into thermal energy. Therefore, a fraction of the gas above a number density threshold of $n > 50 \text{ cm}^{-3}$, a temperature below $T < 2 \times 10^4 \text{ K}$, and within a radius of $r_{\text{acc}} < r < 25 \text{ kpc}$ is locally converted into heat with an efficiency of 5×10^{-6} .

2.2.12. Under the rug: on floors and ceilings

Given the extreme conditions in the central region of the simulation, we limit certain quantities to remain within the reasonable limits of the overall equation system solved (e.g., not entering a relativistic regime). More specifically, within $r < 20 \text{ kpc}$, the velocity is limited to $0.05c$, the Alfvén velocity is also limited to $0.05c$, and the temperature limited to $5 \times 10^9 \text{ K}$, which are implemented as ceilings following the feedback routines. To measure the impact of these limits we tracked the amount of energy being removed from the simulation. Their effective powers were significantly smaller ($\ll 10^3$)

than the AGN feedback and, thus, negligible for the dynamics in the simulation. In addition, we employ a global temperature floor at 10^4 K , which is below the lower end of the cooling tables.

2.3. The simulation suite

A systematic overview of the initial conditions of all current simulations in the XMAGNET suite are given in Table 1. All the cluster simulations, i.e., Perseus-like, a larger one (**Lg**), and a smaller one (**Sm**), use a uniform $2,560^3$ mesh covering the central region whereas in the group simulations, **SPG** and **MPG**, only the $[50 \text{ kpc}]^3$ are covered by a 512^3 mesh at the highest resolution of $\Delta_x \approx 100 \text{ pc}$ in the center. Similarly, the initial velocity perturbations in the group simulation have been scaled down to 30 km/s at 40 kpc scales.

Note that only the Perseus-like cluster results are going to be presented in the following sections of this paper. Results from the large and smaller cluster setups and from the galaxy group simulations will be presented in separate manuscripts.

3. RESULTS

3.1. Self-regulated feedback

All of our simulations reach a state where the entire system self-regulates. The top panel in Fig. 3 shows the AGN power over time. In all cases it takes $\sim 500 \text{ Myr}$ before the AGN turns on for the first time. In these first $\sim 500 \text{ Myr}$ the ICM plasma cools slowly with negligible amounts of cold gas that are required to feed the AGN following the cold mass triggering model.

Once the AGN turns on, its power remains fairly steady at reasonable values between 10^{44} – 10^{45} erg/s in all cases. However, the **WeakMag** and **Hydro** cases tend to be consistently lower at $\sim 10^{44} \text{ erg/s}$ than the **Fiducial** and **WeakCool** cases (with stronger initial fields) at $5 \times 10^{44} \text{ erg/s}$. Only at late times ($> 2.5 \text{ Gyr}$) the power also increases in the **WeakMag** and **Hydro** cases, which can be traced back to AGN activity stimulating the formation of larger amounts of cold gas, cf., the temporal evolution of the total cold ($T < 10^6 \text{ K}$) gas mass in the bottom panel of Fig. 3.

In general, the amount of cold gas present in the cluster depends on both the magnetic field and the cooling table, with an average cold gas mass between 1.5 and 2 Gyr of $2.8 \times 10^{10} M_{\odot}$ (**Fiducial**), $1.3 \times 10^{10} M_{\odot}$ (**WeakMag**), $6.4 \times 10^9 M_{\odot}$ (**Hydro**), and $5.5 \times 10^9 M_{\odot}$ (**WeakCool**), respectively. While **Fiducial** and **WeakCool** contain the largest and smallest amounts of cold gas in the entire simulation volume their AGN powers are comparable, implying that the additional cold gas does not reach the accretion region. The latter

Sim.	B_0 [μG]	Z [Z_\odot]	K_0 [$\text{cm}^2 \cdot \text{keV}$]	K_{100} [$\text{cm}^2 \cdot \text{keV}$]	α_K	r_{200} [Mpc]	M_{NFW} [M_\odot]	c_{NFW}	M_{BCG} [M_\odot]	r_{BCG} [kpc]	M_{SMBH} [M_\odot]
Fiducial	1	1.0	20	110	1.1	1.8	6.6×10^{14}	5.0	2.4×10^{11}	10	1.1×10^9
WeakCool	1	0.3	20	110	1.1	1.8	6.6×10^{14}	5.0	2.4×10^{11}	10	1.1×10^9
WeakMag	10^{-3}	1.0	20	110	1.1	1.8	6.6×10^{14}	5.0	2.4×10^{11}	10	1.1×10^9
Hydro	–	1.0	20	110	1.1	1.8	6.6×10^{14}	5.0	2.4×10^{11}	10	1.1×10^9
FiducialLg	1	1.0	15	110	1.1	2.28	1.3×10^{15}	5.0	1×10^{12}	7	7×10^9
WeakMagLg	10^{-3}	1.0	15	110	1.1	2.28	1.3×10^{15}	5.0	1×10^{12}	7	7×10^9
HydroLg	–	1.0	15	110	1.1	2.28	1.3×10^{15}	5.0	1×10^{12}	7	7×10^9
FiducialSm	1	1.0	1.53	150	1.1	1.1	1.5×10^{14}	5.0	5×10^{11}	7	5×10^9
WeakMagSm	10^{-3}	1.0	1.53	150	1.1	1.1	1.5×10^{14}	5.0	5×10^{11}	7	5×10^9
HydroSm	–	1.0	1.53	150	1.1	1.1	1.5×10^{14}	5.0	5×10^{11}	7	5×10^9
FiducialMPG	1	1.0	1.3	150	1.05	2	4.4×10^{13}	9.5	1.2×10^{11}	1.2	4.6×10^8
HydroMPG	–	1.0	1.3	150	1.05	2	4.4×10^{13}	9.5	1.2×10^{11}	1.2	4.6×10^8
FiducialSPG	1	1.0	1.5	400	1.05	1.8	4×10^{13}	7.5	2×10^{11}	1.6	2.6×10^9
FiducialCcSPG	1	1.0	1.5	200	1.05	1.8	4×10^{13}	7.5	2×10^{11}	1.6	2.6×10^9
HydroSPG	–	1.0	1.5	400	1.05	1.8	4×10^{13}	7.5	2×10^{11}	1.6	2.6×10^9
HydroCcSPG	–	1.0	1.5	200	1.05	1.8	4×10^{13}	7.5	2×10^{11}	1.6	2.6×10^9

Table 1. Key differentiating parameters of all simulations: The initial magnetic field strength is the RMS value of B_0 on 100 kpc scales, Z is the metallicity of the cooling table, K_0 and K_{100} the specific entropies in the center and at $r = 100$ kpc, respectively, α_K is slope of the entropy profile, r_{200} is the virial radius where the initial density of $\rho(r_{\text{ref}}) = 9.47 \times 10^{-29} \text{ g/cm}^3$ is fixed, $M_{\text{NFW}} (= M_{200})$, M_{BCG} , and M_{SMBH} are the dark matter halo, BCG, and SMBH masses, c_{NFW} is the concentration parameter, and r_{BCG} is the scale radius of the Hernquist profile for the BCG.

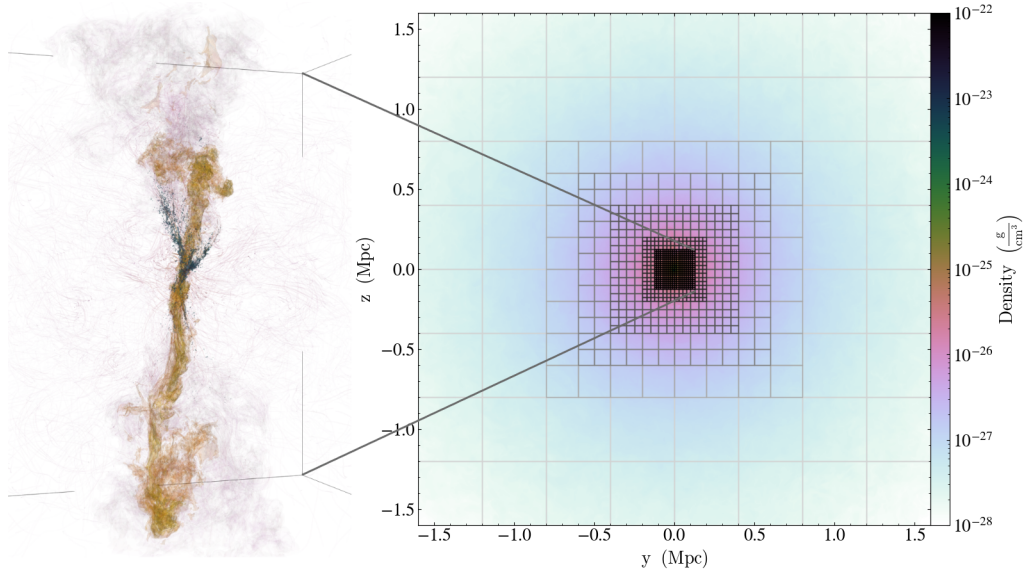


Figure 2. Illustration of the mesh (excluding the root mesh covering a $[6.4 \text{ Mpc}]^3$ domain) used in the cluster simulations. Each square is a cube containing 128^3 cells for a total of ≈ 36 billion cells. Overall, 6 levels of refinement are used so that the innermost $[250 \text{ kpc}]^3$ is covered by a uniform 2560^3 mesh with $\Delta_x = 100 \text{ pc}$. The volume rendering of the central region highlights jet material in orange colors and cold gas in dark blue.

is likely related to the instantaneous stellar feedback that is converting more cold gas into thermal energy in the Fiducial case, cf., the second panel in Fig. 3.

The resulting densities in the launching cells is typically $\mathcal{O}(10^{-26}) \text{ g/cm}^3$.

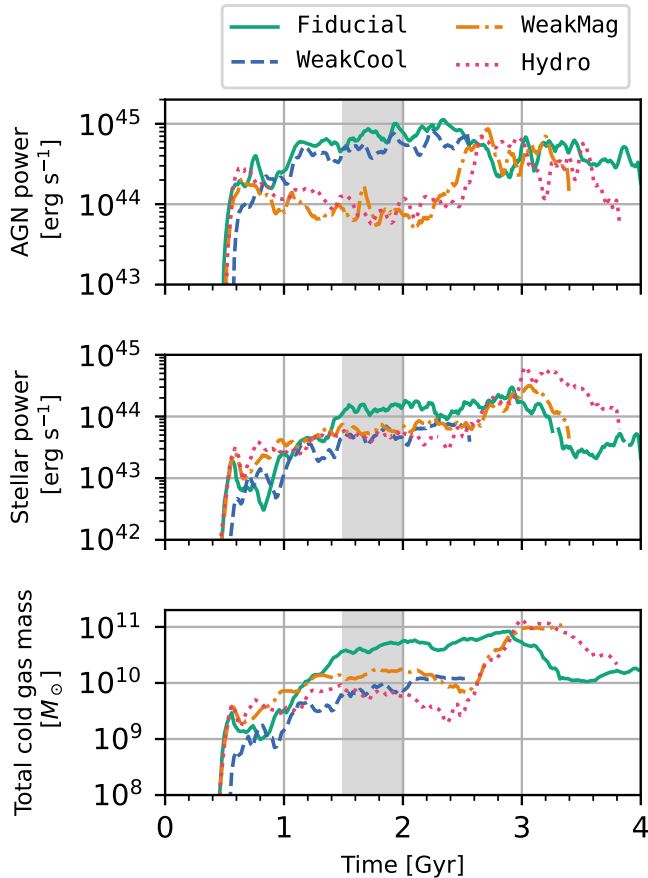


Figure 3. From top to bottom: Temporal evolution of the AGN feedback power, instantaneous stellar feedback power (excluding Type Ia SNe), mass deposition rate, and total amount of cold gas. The extend of the lines indicate the runtime of the simulations. Given the 10x higher output frequency (every 2 Myr) in the first two panels the data is smoothed over 50 Myr using a box filter. The shaded region illustrates the time interval that is used to quantify averaged properties in other figures.

Overall, the AGN power only exhibits limited variability and no clear “duty cycles” are directly visible from the temporal evolution of the power itself. However, individual outbursts are still clearly visible as illustrated in Fig. 4. The panels show three volume rendering of the passive tracer injected with the jet at snapshots 40 Myr apart. In the first panel, a jet is clearly visible extending in the top right direction. 40 Myr later this jet event has been dissipated while another jet starts to form towards the top left direction. Finally, the last panel (another 40 Myr later) illustrates the new jet extending even further outwards. It also shows the formation of cold gas following the direction of the initial jet, highlighting the link between jet activity and the formation of cold gas.

For an overall impression of the general differences in morphologies between the simulations, Fig. 5 shows a 10 kpc deep projection of both hot and dense gas. **Fiducial** and **WeakCool** both exhibit extended filamentary structures of cold gas. Overall, the **Fiducial** case is more dynamic with more cold gas being available and visible at larger distances from the center. Similarly, the jet in the **Fiducial** case is visibly stronger and more dynamic than in the **WeakCool** case. **WeakMag** and **Hydro** are in stark contrast to those dynamics. In these latter simulations the cold gas is mostly confined to a disk around the center (indicating that weak magnetic fields are not enough to prevent the formation of a disk as in the pure hydrodynamics case). Moreover, the lower jet power in these cases is clearly visible and, in the absence of extended cold gas to interact with, the jet itself is much narrower and more closely aligned with its original launching direction.

3.2. Thermodynamics and energetics

The mass-weighted temperature histograms versus radius from the cluster center are shown in Fig. 6. Down to cluster-centric radius of 10 kpc the average temperature does not differ much between setups and is dominated by the bulk mass of the hot 10^7 – 10^8 K ICM. The cold gas distribution, however, differs significantly between runs with (traces of) cold gas visible up to $r \sim 150$ kpc in the **Fiducial** case, $r \sim 100$ kpc in the **WeakCool** case, $r \sim 30$ kpc in the **WeakMag** case, and $r \sim 20$ kpc in the **Hydro** case. This also applies to intermediate-temperature gas visible as vertical streaks extending down from the hot, bulk ICM at different radii depending on the run. Thus, both magnetic fields and the efficiency of the cooling impact the extent of cold gas with the magnetic fields having a stronger effect – though the impact may also be indirect, cf., the varying AGN powers. The overall behavior is equally visible in the time-averaged histograms over 500 Myr shown in the bottom panels of Fig. 6.

From an even higher-level point of view, Fig. 7 shows that the median radial profiles over 500 Myr of the entropy and cooling time are indistinguishable between the runs down to 30 kpc. Within 30 kpc the situation is more dynamic between the different runs with entropies of order unity $\text{keV}\cdot\text{cm}^2$ and cooling times between 0.1–1 Gyr. No clear trend that differentiates between the metallicities of the cooling table nor the initial magnetic field strength is visible between $1 \leq r \leq 10$ kpc.

The overall energy balance is depicted in Fig. 8 based on the median radial profiles of the sonic Mach number (as a proxy for the kinetic energy over thermal pressure), the Alfvénic Mach (as proxy for the kinetic over mag-

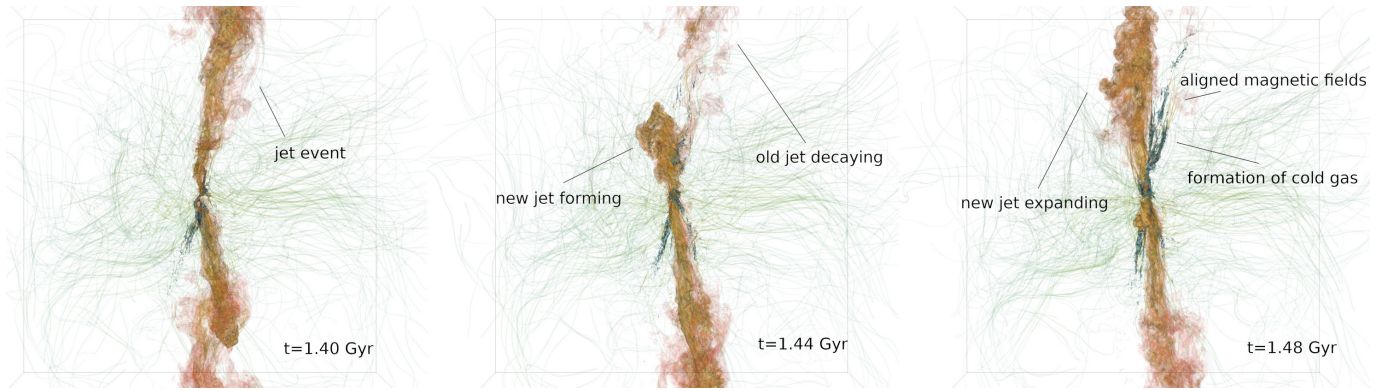


Figure 4. Volume renderings of the central $[200 \text{ kpc}]^3$ in the **Fiducial** simulation at $t = \{1.40, 1.44, 1.48\}$ Gyr highlighting jet variability on short timescales (here 40 Myr apart). Yellow colors indicate jet material (passive tracer concentration), dark blue colors show cold, $\approx 10^4$ K, gas, and green lines illustrate magnetic fields.

netic energy), and plasma beta (as thermal pressure over magnetic energy/pressure). The Alfvénic Mach is comparable within $r \leq 4 \text{ kpc}$ (dropping from several tens to several few) for all simulations that include magnetic fields. Then it continues to decline, eventually becoming sub-Alfvénic beyond $r \gtrsim 100 \text{ kpc}$ in the **Fiducial** and **WeakCool** case whereas for **WeakMag** it increases again rapidly to ~ 200 , i.e., to a highly super-Alfvénic state. This is also reflected in the plasma beta. For **WeakCool** it remains approximately constant within $r \leq 500 \text{ kpc}$ with values of several hundreds up to 1000. At $r > 10 \text{ kpc}$ this also applies to the **Fiducial** case; however, at small distances from the center the plasma beta drops to $\mathcal{O}(10)$. Again, the **WeakMag** simulation stands out with plasma betas reaching 10^5 beyond $r > 10 \text{ kpc}$. Given the $1/B^2$ scaling of the plasma beta and an initial difference in B_0 of 10^3 between the **Fiducial/WeakCool** and **WeakMag** case, this already gives a first indication of an effective magnetic field amplification that is further discussed in Subsection 3.4.

Lastly, the radial profiles of the sonic Mach number shown in the top panel of Fig. 8 indicate that the innermost region $r \lesssim 8 \text{ kpc}$ is highly super-sonic with Mach numbers reaching $\mathcal{O}(10)$, which then transitions to become subsonic ($\mathcal{O}(0.1)$). In general, the **WeakMag** and **Hydro** case are effectively indistinguishable with a sharp transition between the super- and sub-sonic regime. **Fiducial** and **WeakCool** exhibit a smoother transition with the former only occurring at larger radii ($8 \lesssim r \lesssim 80 \text{ kpc}$ versus $3 \lesssim r \lesssim 30 \text{ kpc}$). This is tied to the different cold gas distribution given the mass weighting in the radial profiles. A more detailed picture is displayed in Fig. 9, where the 2D histograms of sonic Mach number versus radius are shown for all simulations. An almost bimodal distribution is visible with a high (Mach ~ 10) component consisting of both the jet (fast and hot material) and cold gas (resulting in a low

sound speed). This also explains why the sonic Mach number is more extended in the **Fiducial** case than for the other ones, cf., the temperature profiles (and extent of cold gas) in Fig. 6.

3.3. Turbulent power spectra

The large uniform resolution in the central region of our simulations allows us to calculate the power spectra using standard methods typically applied in idealized turbulent boxes.⁵ All spectra discussed cover the central $[200 \text{ kpc}]^3$ with a resolution of $2,048^3$ cells.

Fig. 10 shows the turbulent specific kinetic energy, kinetic energy density, and magnetic energy density power spectra at different times. The times have been chosen to correspond to peak AGN power ($t = \{1.94, 2.32\}$ Gyr) and low AGN power in between ($t = \{1.86, 2.06\}$ Gyr). It is immediately visible that the AGN is linked to the velocity fluctuations (i.e., the specific kinetic energy power spectrum). At higher AGN activity there is more power on all scales – especially between characteristic scales of $2 \lesssim \ell \lesssim 20 \text{ kpc}$. At the two times with lower AGN activity (which surround the first peak time) the spectra are effectively identical, highlighting the different phases of AGN activity and their impact on the velocity structure. Moreover, the activity also impacts the shape of the power spectra, cf., the bottom left panel in Fig. 10 which shows the compensated spectra and for which a clear break in spectral slope is visible at $t = 1.94 \text{ Gyr}$. This potentially also applies to the kinetic energy density spectra, i.e., the ones based on $\mathbf{w} = \sqrt{\rho}\mathbf{u}$ taking

⁵ We used the energy transfer analysis framework (<https://github.com/pgrete/energy-transfer-analysis>) to calculate the spectra (Grete et al. 2017), which assumes periodic boxes. Technically, a central cutout from our current simulations is not periodic. However, given the smooth, almost radial symmetric properties at $r \gtrsim 100 \text{ kpc}$ the cutouts are effectively symmetric introducing only very limited noise close the grid cutoff scale.

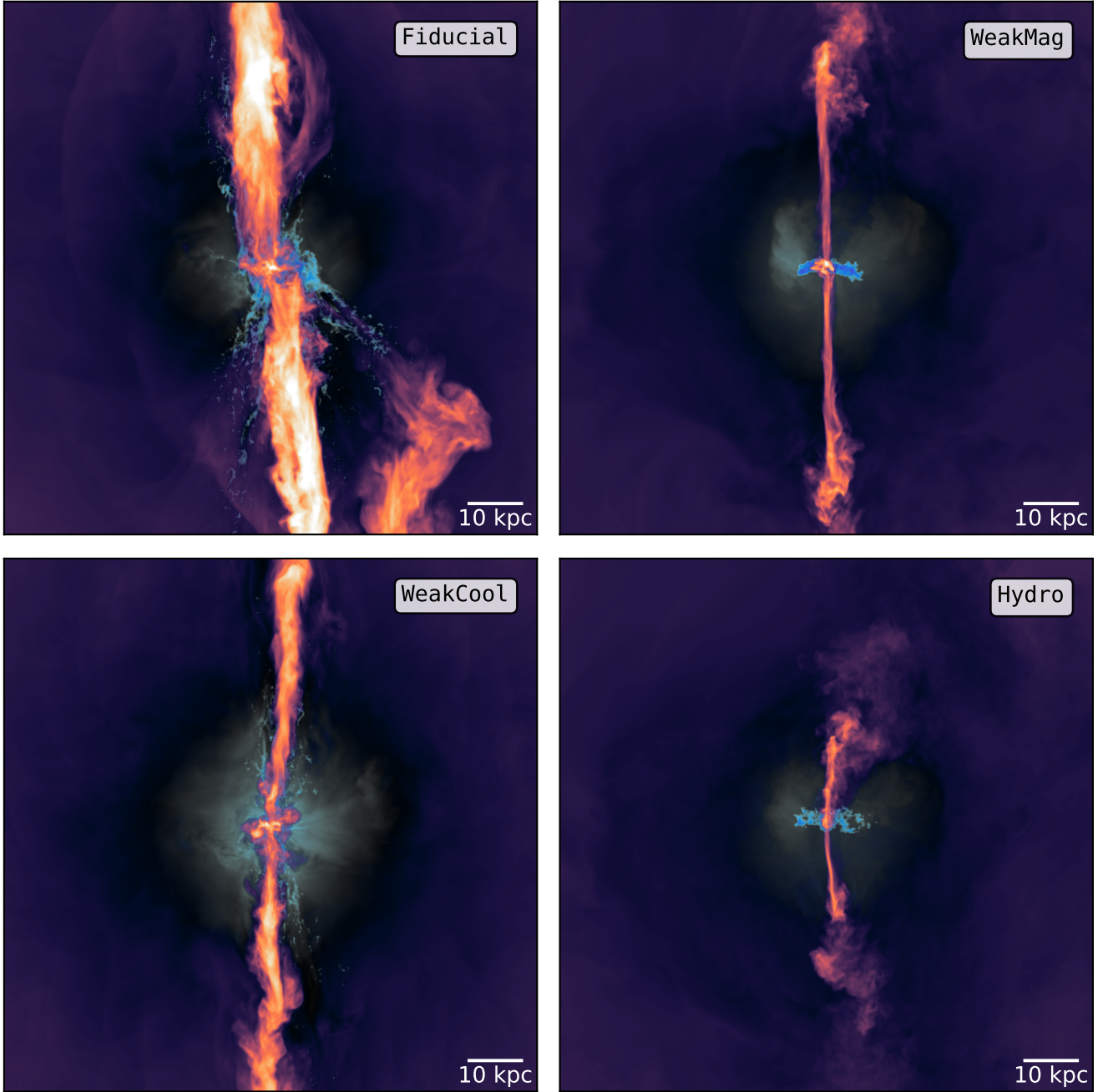


Figure 5. Projections with a depth of 10 kpc of the central $([-50, 50] \text{kpc})^2$ at $t = 1.72 \text{ Gyr}$ highlighting the key dynamical differences between the different simulations (i.e., the AGN power, and amount and distribution of cold gas). Dense gas is shown in bright blue colors and hot gas in red colors.

density fluctuations into account. However, the differences in these spectra are much more subtle and barely visible. Overall, the kinetic energy density spectra are effectively identical, as are the magnetic energy density spectra (right panels of Fig. 10). From a general energy balance point of view the inset in Fig. 10 compares kinetic and magnetic energy density spectra at the same time. On effectively all scales (and particularly on small

scales $\ell \lesssim 10 \text{ kpc}$) the gas motion is dominated by velocity fluctuations.

In addition to temporal variations, there also exist variation with respect to the different simulation setups. Fig. 11 shows the median spectra (between 1.5–2 Gyr) of all four configurations that exhibit extended regimes of power-law scaling. The specific kinetic energy spectra (left panel) is effectively identical between runs with

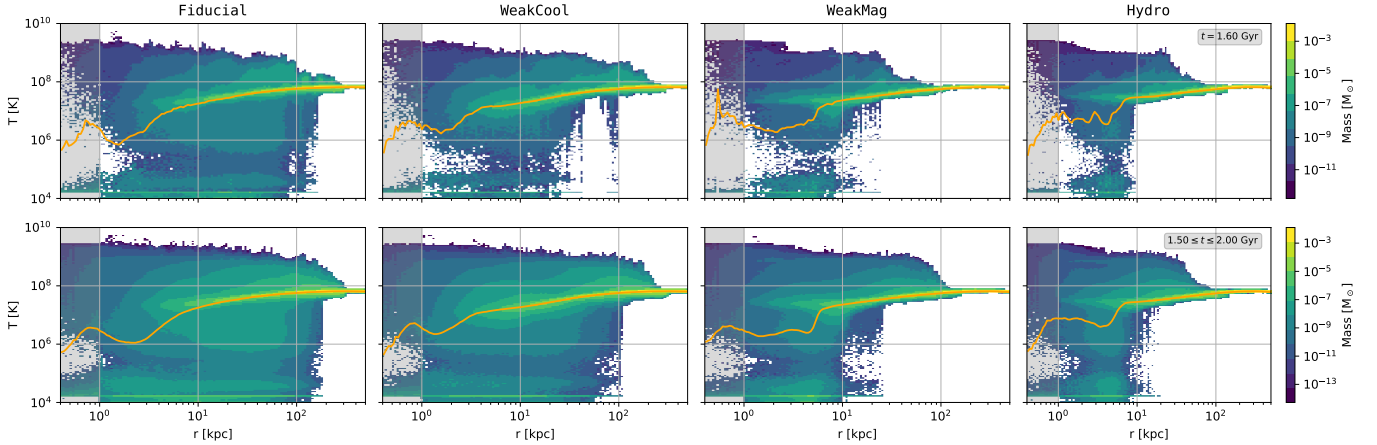


Figure 6. Mass-weighted temperature histograms at $t = 1.6$ Gyr (top panels) and averaged between $1.5 \leq t \leq 2.0$ Gyr (bottom panels) of all simulations. The orange lines indicate the mass-weighted mean temperature versus radius. The gray shaded region illustrates the innermost kpc for which the statistics should be interpreted with care given the various active AGN model components.

similar initial magnetic field strength (and, thus, AGN power), i.e., **Fiducial** and **WeakCool**, and **WeakMag** and **Hydro**. Similar to the instantaneous spectra, the latter two have less power on all scales. Moreover, a hint of a break in the scaling is visible around $\ell \sim 10$ kpc with a steeper spectrum on larger scales. The impact of the different cooling tables (and initial magnetic field strength) is clearly visible in the kinetic energy density power spectra in the center panel of Fig. 11. Again, **WeakMag** and **Hydro** are indistinguishable from each other. However, **Fiducial** and **WeakCool** only follow each other down to scales of $\ell \gtrsim 5$ kpc. At those scales the spectrum of **WeakCool** becomes significantly steeper whereas the **Fiducial** one extends further, indicating an impact of the cold (high density) gas dynamics on small scales. Finally, the magnetic energy power spectrum in the right panel of Fig. 11 is again similar between the **Fiducial** and **WeakCool** case, with slightly more power in the magnetic field fluctuations on scales $\ell \lesssim 10$ kpc in the **Fiducial** case with stronger cooling. The **WeakMag** magnetic energy spectrum does not exhibit a power law scaling regime, peaks around $\ell \sim 10$ kpc, and the fluctuation generally remain weaker on all scales compared to the other cases. These differences are presented further in the following subsection.

3.4. Magnetic fields

The radial profiles of the magnetic field strength at various times and intervals are illustrated in Fig. 12. Independent of setup the magnetic fields reach strengths of several 10^{-5} G within $r \lesssim 10$ kpc even in the **WeakMag** case and do not vary significantly after 1.5 Gyr. At these late times, the fields towards larger radii in the **Fiducial** and **WeakCool** cases continuously decrease

smoothly down to 10^{-5} G at $r \sim 100$ kpc whereas in the **WeakMag** case they almost follow two step functions down to a few 10^{-7} G at $r \sim 8$ kpc and then another $> 10\times$ decrease around $r \sim 100$ kpc. Beyond $r \gtrsim 100$ kpc the fields even decay from their initial values, making $r \sim 100$ kpc a relevant scale out to which the AGN actively modifies the magnetic field configuration. At smaller radii it takes several hundreds of Myr for the profiles to stabilize even though the initial magnetic field growth is fast.

This growth is further illustrated in Fig. 13 where instantaneous magnetic field power spectra are plotted around the first AGN outburst for the **Fiducial** and **WeakMag** case (left panel) along with the magnetic field amplification at scales of $\ell = \{1, 10, 20\}$ kpc for the first 1.25 Gyr. For the stronger initial fields in **Fiducial** the amplification of the fields occurs gradually at large scales (by a factor of $\sim 4\times$ over ~ 500 Myr at $\ell = \{10, 20\}$ kpc) and faster on smaller scales ($4\times$ within ~ 150 Myr at $\ell = 1$ kpc). The magnetic field amplification in the **WeakMag** case is much more extreme. On all reference scales the magnetic field strength increases by $> 100\times$ in $\lesssim 100$ Myr and on the smallest scale ($\ell = 1$ kpc) even by $\gtrsim 100\times$ within just 20 Myr. In the **WeakMag** case the field growth continues, peaking at $\gtrsim 1000\times$ on the small scales.

3.5. AGN area of influence

As presented in the preceding subsection, the AGN feedback impacts the magnetic fields out to $r \lesssim 100$ kpc, and, as shown in Subsection 3.2, the presence and/or formation of cold gas to various radii depends on the setup. To understand where the plasma of the AGN jet

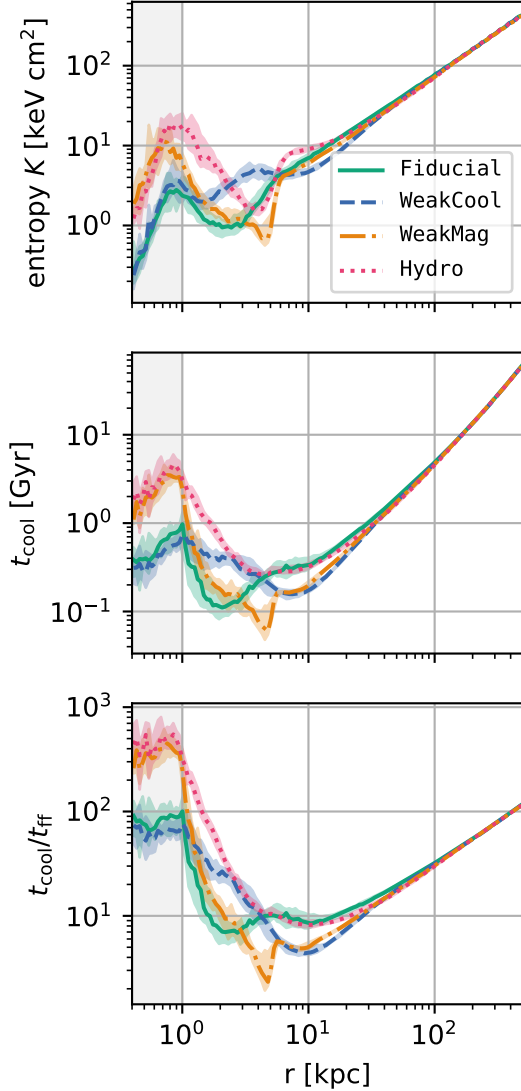


Figure 7. Median and inter quartile ranges (over time between $1.5 \leq t \leq 2.0$ Gyr) of the mass-weighted mean entropy (top), cooling time (center), and cooling over freefall time (bottom). Here and in subsequent plots, the gray-shaded region denotes the innermost kpc for which our results strongly depend on the AGN model. Plots show that $\min(t_{\text{cool}}/t_{\text{ff}})$ stays within 5–20 for all the runs within $r < 50$ kpc allowing for formation of extended cold gas filaments.

ends up, the passive tracer concentration is shown in Fig. 14 for spherical θ angle versus radius.

AGN with higher powers (Fiducial and WeakCool) push tracer material to higher altitudes (up to ~ 300 kpc at 2 Gyr compared to ~ 150 kpc for WeakMag and Hydro). Moreover, for Fiducial and WeakCool the tracer concentration at radii larger than several tens of kpc is limited to low and high values of θ . This means that the material is mostly concentrated around the jet axis. There is no large-scale circulation through the midplane

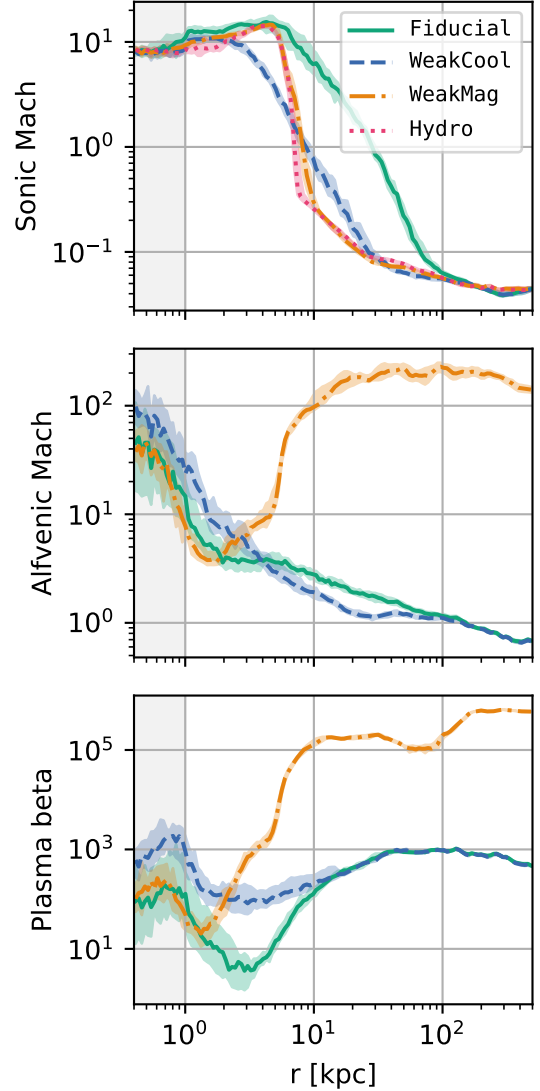


Figure 8. Median and inter-quartile ranges (over times $1.5 \leq t \leq 2.0$ Gyr) of the mass-weighted mean sonic Mach number (top), Alfvénic Mach number (center), and plasma β (bottom). Note the stark difference in the plasma β and Alfvénic Mach number for the weak magnetic field ($B = 0.001\mu$ G) run compared to the fiducial run with $B = 1\mu$ G indicates an effective magnetic field amplification owing to the $1/B^2$ scaling of the plasma β and an initial difference in B_0 of 10^3 between the Fiducial/WeakCool and WeakMag case.

from larger radii. In contrast, the WeakMag and Hydro cases show a more isotropic distribution of the tracer material both around the center (a few kpc scales) and around 70–100 kpc scales.

4. DISCUSSION

4.1. Cluster self-regulation

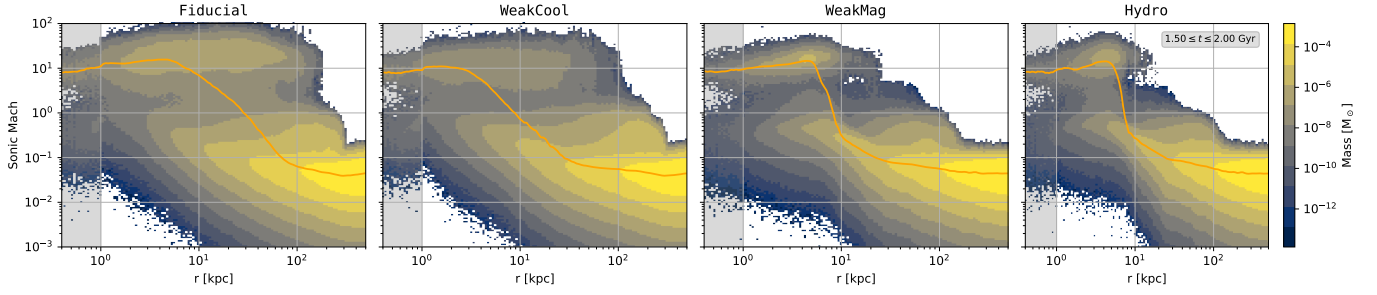


Figure 9. Mass-weighted sonic Mach number histograms averaged between $1.5 \leq t \leq 2.0$ Gyr of all simulations. The orange lines indicate the mass-weighted mean sonic Mach number versus radius.

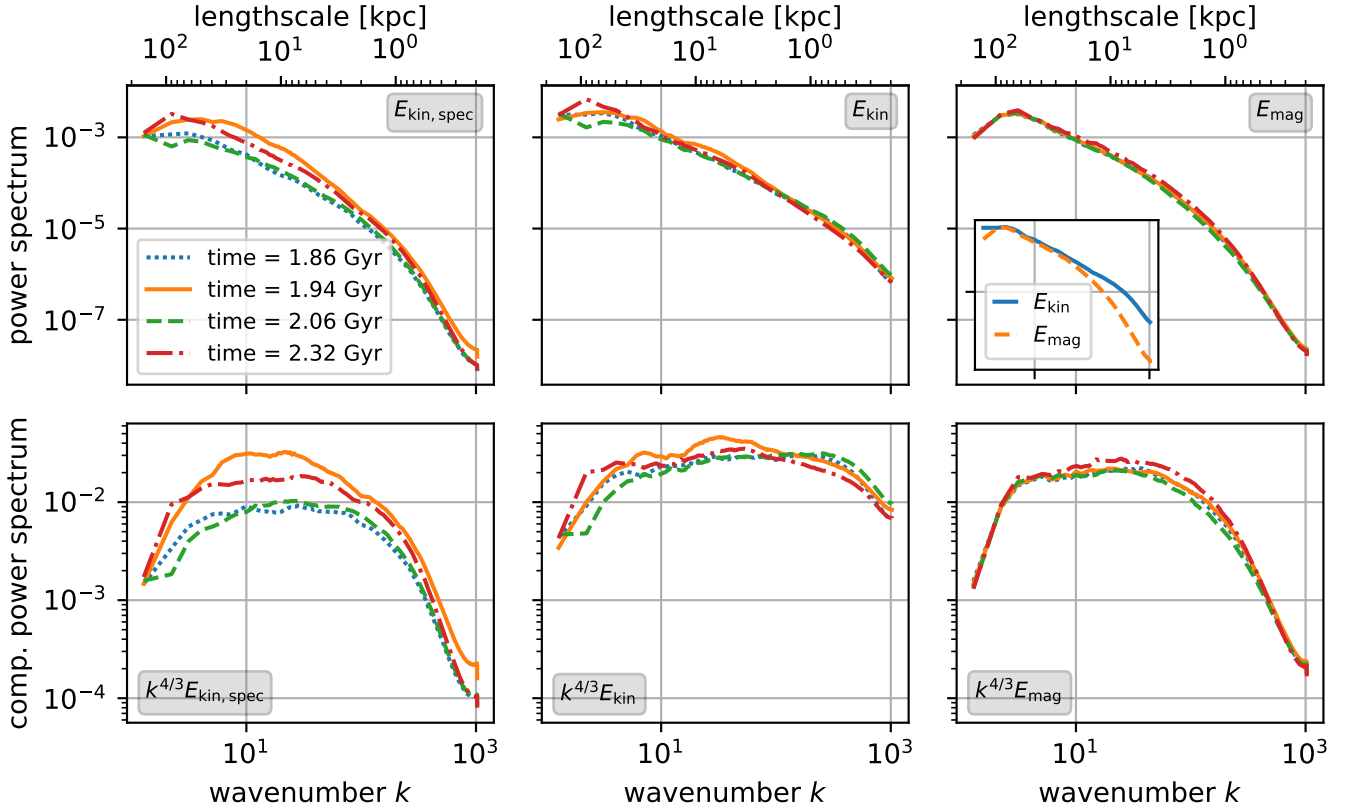


Figure 10. Instantaneous turbulent power spectra at various times of the specific kinetic energy (left), the kinetic energy density (based on $\mathbf{w} = \sqrt{\rho}\mathbf{u}$, center panel), and magnetic energy density (right) in the **Fiducial** simulation. The raw, i.e., uncompensated spectra are shown in the top panels whereas the spectra in the bottom panels are compensated by $k^{1.2}$, $k^{1.1}$, and $k^{1.2}$, respectively. The inset in the top right panel shows the spectra of kinetic energy density and magnetic energy density at $t = 1.86$ Gyr. The axes ranges in the inset are the same as in the larger panels.

The clusters discussed in Section 3 all self-regulate, in the sense that the energy feedback from AGN and stars offsets the radiative cooling in the cluster core (defined for the purpose of this discussion to be the region within $\simeq 100$ kpc of the cluster center). The feedback power lies between $10^{43} - 10^{45}$ erg/s (as can be seen in Figure 3). The simulations with high magnetic fields (i.e., consistent with observed cluster cores) typically have roughly a factor of 4 – 6 higher sustained levels of

AGN feedback than the low magnetic field or hydrodynamic (zero-field) simulations during the first $\simeq 2$ Gyr after the AGN starts. This corresponds to times of roughly 0.4 – 2.4 Gyr⁶. In spite of significantly different AGN power during that time, the total amounts of

⁶ We note that the hydrodynamical and weak initial field MHD runs abruptly form a large amount of cold gas at $t \sim 2.5$ Gyr, and hence we generally focus on evolution prior to that time.

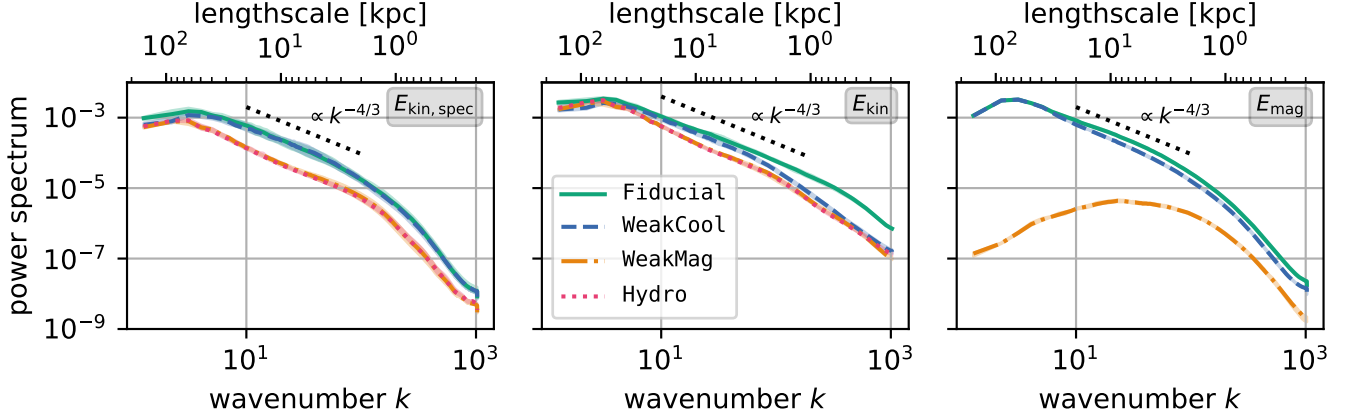


Figure 11. Median turbulent power spectra (with IQR in shaded regions) of the specific kinetic energy (left), the kinetic energy density (based on $\mathbf{w} = \sqrt{\rho}\mathbf{u}$, center panel), and magnetic energy density (right) between 1.5–2 Gyr for all four simulations. The slopes are just given for reference and do not represent physical models.

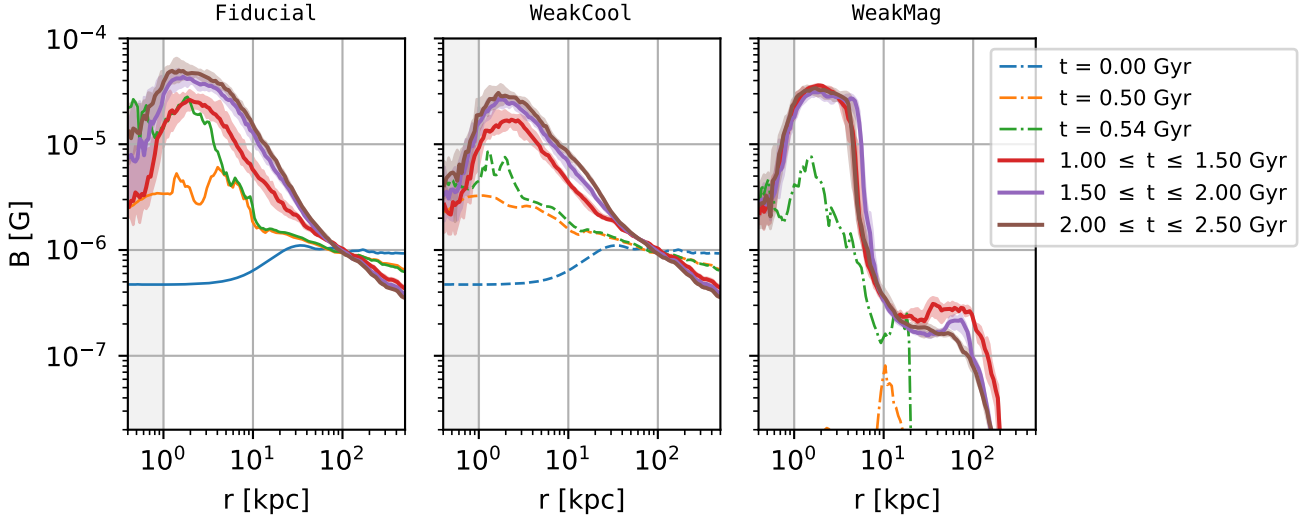


Figure 12. Mass-weighted magnetic field strength versus radius at various times and intervals (using the median and interquartile ranges as colored extents) for the **Fiducial**, **WeakCool**, and **WeakMag** simulation (from left to right).

cold gas in all four simulations are similar, even though the high cooling/high field “fiducial” run ultimately produces more cold gas than the other simulations. Examination of Figure 6 suggests that this is primarily caused by the distribution of cold gas rather than the total amount – i.e., the strong field/strong cooling run has much more cold gas at large radii than the other simulations.

All of the AGN in our simulations operate continuously – i.e., they do not have a discernable “duty cycle” where the AGN transitions between a state of high activity and one where it is either completely turned off or in a much lower state of activity. This is possibly consistent with observations, which use a variety of means to estimate the duty cycle. Observations by [Vantyghem et al. \(2014\)](#) using primarily X-ray observations suggest

a relatively low duty cycle, where the AGN is in its high state (i.e., where the AGN is injecting energy at rates comparable to the cluster’s X-ray luminosity) significantly less than half of the time. This result is in tension with a volume-limited X-ray sample of clusters by [Panagoulia et al. \(2014\)](#), who estimate a duty cycle of $\approx 60\%$ for clusters with central cooling times of ≤ 3 Gyr and $\gtrsim 80\%$ for clusters with a central cooling time of ≤ 0.5 Gyr. This latter result is in agreement with our simulated clusters, which all have central cooling times of ≤ 0.5 Gyr in the central 20 kpc (central panel of Figure 7). More recent radio observations of AGN jet-driven bubbles in the intracluster medium using LOFAR that include models of spectral aging for the electron synchrotron emission suggests that the AGN

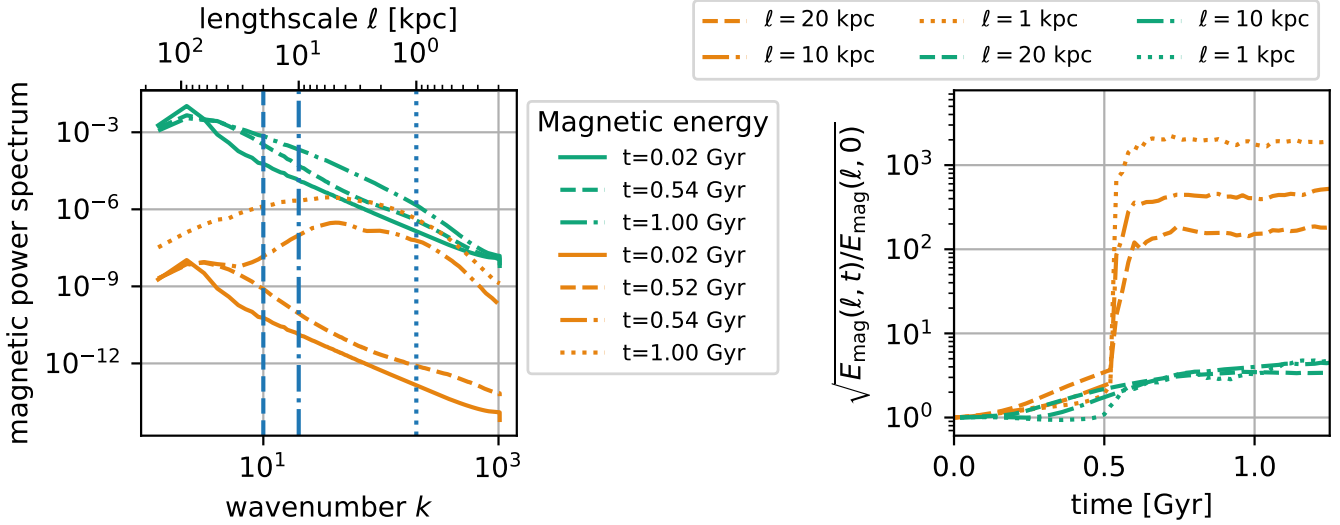


Figure 13. Left: Magnetic energy spectra of the **Fiducial** (green) and **WeakMag** simulation (orange) at various times. The vertical blue lines indicate scales for which the power is plotted over time in the right panel (normalized to the initial value at the particular scale).

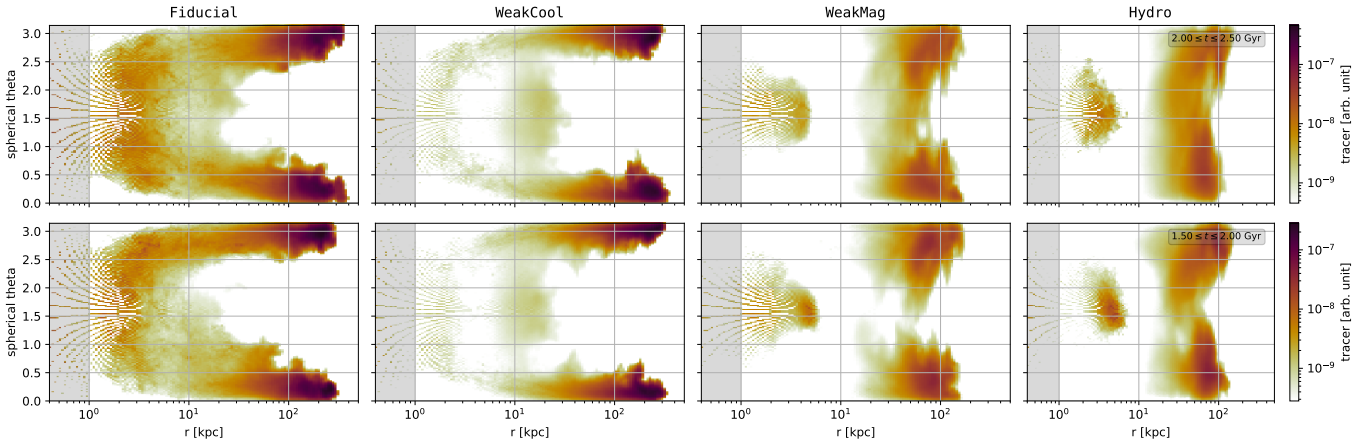


Figure 14. Tracer concentration in spherical polar coordinate θ versus radius at $t = 1.6$ Gyr (top panels) and averaged between $1.5 \leq t \leq 2.0$ Gyr (bottom panels) of all simulations highlighting more concentrated jet material at higher altitudes in the **Fiducial** and **WeakCool** cases, and a more isotropic distribution in the **WeakMag** and **Hydro** cases.

they observe has had a duty cycle close to unity in the past $\simeq 100$ Myr (Biava et al. 2021). These results are generally consistent with the behavior we see in all of our simulations. We note, however, that the gas accretion timescale that we use ($T_{acc} = 100$ Myr) is relatively long and may smooth out accretion behavior. Future simulations with varied accretion timescales will shed light on whether the high duty cycle that we observe is physical or numerical in nature.

The cluster entropy profiles show that all of the clusters are roughly consistent with X-ray observations, with central entropies in the 1–10 keV range and central cooling times (within 10 kpc) in the 0.1–1 Gyr ranges. The central entropy of the strong magnetic field runs tend to

flatten toward the center, and the weak magnetic field and hydrodynamical runs tend to be higher near the center. We infer that this has to do with the magnetic fields, but the causal mechanism is unclear. The region within 1.0 kpc of the cluster center is within the AGN accretion and thermal feedback regions, and thus any thermodynamic quantities that are measured should be interpreted with caution. The difference in the entropy profile near the center between the strong magnetic field cases and the hydro and weak magnetic field cases is because there is more dense gas near the jet source region in those cases. This can be seen in Figure 7, where the hydro/weak field cases have higher t_{cool} within $r \lesssim 2$ kpc because that quantity depends inversely on density.

In terms of comparisons to prior simulation work relating to self-regulated clusters, we see that in terms of bulk behavior our results are consistent with those of Meece et al. (2017), who use a very similar triggering and jet injection mechanism, although with $2\times$ coarser spatial resolution (and effectively significantly worse effective spatial resolution given that they use the ZEUS hydro method, which uses artificial viscosity and has significant smoothing and mixing – see O’Shea et al. (2005) for information).

Our results differ from previous results of self-regulating galaxy clusters. Hydrodynamic simulations of idealized clusters including cold gas-triggered AGN, such as those performed by Gaspari et al. 2012; Prasad et al. 2015, Li et al. (2015) and Meece et al. (2017), typically show a greater variability in AGN energies and large-scale cyclic behavior on \sim Gyr time scales. On the other hand, Ehlert et al. (2023) perform simulations of self-regulated magnetized AGN feedback in cool-core clusters and see behavior that is more similar to our results – i.e., the jets in their simulations, regardless of the precise details of jet momentum density or triggering mechanism, are continuously on. An interesting intermediate case is provided by Yang & Reynolds (2016), who use cold-gas triggered hydrodynamical jets in an initially magnetized medium. This work shows highly variable AGN energies but no indication of Gyr-scale patterns. It is unclear whether the difference in jet behavior between hydrodynamical and magnetohydrodynamical simulations of self-regulated AGN feedback is primarily caused by the magnetic fields themselves or by other feedback parameters. For example, the momentum density of the jet affects the jet behavior – see, e.g., the discussion in Section 7.2 of Prasad et al. (2020), Section 5.1 of Prasad et al. (2022), and Section 3 of Weinberger et al. (2023). In general, lighter jets are more easily contained at smaller cluster-centric radii and are also more easily deflected by cold gas than heavier jets. This may result in the simulated cluster’s center displaying less variability in its thermodynamic state than for heavier jets.

Conversely, some studies have shown that jet precession or reorientation might play a role in the dynamics of the cold phase. In Beckmann et al. (2019), rapid re-orientation of the jets on timescales of a few tens of Myr pushes the cold phase outwards in a nearly isotropic way, effectively shutting off the fueling of the AGN for a few tens of Myr and possibly resulting in the alternation between heating and cooling dominated phases.

4.2. On the cluster magnetic fields

The calculations that include magnetic fields show that AGN feedback has a significant impact on the magnetic fields in our simulated clusters. While the AGN injects a substantial amount of energy into the cluster only 1% of it is magnetic energy, with the rest being distributed between kinetic (74%) and thermal energy (25%). Over the duration of the simulation this means that for a jet with a sustained total energy injection rate of 10^{44} (10^{45}) erg/s, the total magnetic energy injected into the system per billion years is $\simeq 3 \times 10^{58}$ (3×10^{59}) ergs. The region of AGN influence is effectively within $\simeq 100$ kpc of the cluster center, and the total amount of magnetic energy contained within that volume is $\simeq 1.7 \times 10^{58}$ ergs (Fiducial), $\simeq 9.9 \times 10^{57}$ ergs (WeakCool), and $\simeq 4.3 \times 10^{56}$ ergs (WeakMag) – larger than the original magnetic energy contained within that region ($\simeq 4.9 \times 10^{57}$ ergs for the Fiducial/WeakCool case; $\simeq 4.9 \times 10^{51}$ ergs for the WeakMag case), but not larger than the amount of magnetic field energy injected by the AGN.

The weak vs. strong initial magnetic field simulations inject different amounts of magnetic energy – roughly a factor of six integrated over the time range of 0.4 – 2.4 Gyr. Beyond this bulk difference in total energy injection, the differences between the simulations shown in Figure 12 are informative. The “strong B” cases with different cooling rates are very similar in amplitude and shape, though the stronger cooling case has somewhat higher overall field strengths within 100 kpc at later times (by roughly a factor of two). There is clear evidence of field amplification out to several tens of kpc. This is an interesting contrast to the weak initial magnetic field case, where the fields are comparably large to the strong initial magnetic field case only within $\simeq 5$ kpc of the cluster center, and are much weaker at larger radii (and fall off tremendously outside of $\simeq 100$ kpc).

Since the amount of magnetic fields produced by the AGN in these three simulations are effectively the same, we can draw two conclusions from this. First, it seems likely that most of the magnetic field energy coming from the AGN jet is either deposited at large cluster-centric radii or dissipated away. The argument that much of the injected magnetic energy is deposited at large radii is supported by Figure 14, which shows where the “tracer fluid” injected with the AGN can be found. This fluid is deposited in the same cells where the magnetic field is deposited, and thus is a good proxy for where the injected fields ultimately reside. However, the ICM at large radii is much less dense than at low radii, and the flux-frozen magnetic fields will adiabatically lower in amplitude, making it difficult to differentiate between the origins. It is also possible that the

magnetic energy in the jet is turned into kinetic energy, and ultimately dissipated. It is likely that this is a sub-dominant process, however, because the initial configuration of our injected magnetic field is a loop and thus it is unclear how the injected magnetic fields would exert force on the ICM to transfer magnetic energy into kinetic energy.

In addition, we expect that the magnetic field is additionally amplified by small scale dynamo action (Brandenburg & Subramanian 2005; Rincon 2019). This is particularly visible in the **WeakMag** case in the magnetic energy spectra in Fig. 11 where the magnetic spectrum peaks at $\simeq 10$ kpc scales. Thus, the strongest coherent field exists on this scale, which is significantly larger than the injection scale. At the same time, the fields are amplified $> 100\times$ within $\simeq 100$ kpc in the **WeakMag** case, indicating significant overall magnetic field amplification (see Fig. 12). Similarly, when comparing the simulations with identical initial field strength (**Fiducial** and **WeakCool**), the specific kinetic energy spectra, i.e., the raw velocity fluctuations perfectly agree on average (see left panel of Fig. 11), whereas there is consistently less power in magnetic fluctuation on scales $\lesssim 20$ kpc in the **WeakCool** case compared to the **Fiducial** case. Assuming that the velocity fluctuations reached a stationary state in both cases, the additional power injected by the AGN in the **Fiducial** case has been converted to magnetic energy dynamically, i.e., eventually through dynamo action. A future energy transfer analysis following Grete et al. (2017) will be able to quantify the different processes.

Finally, we note that the fields outside of $\simeq 100$ kpc from the cluster core can be seen to weaken over time, as can be seen most clearly in the left and center panels of Figure 12. This is unlikely to come from significant evolution of the intracluster medium at those scales, since the cooling times at large scale are $\gg 1$ Gyr and the ICM entropy profile is stable (see the middle and top panels of Figure 7, respectively). We note that the initial conditions in our MHD simulations include an initial magnetic field that is perturbed on scales between 50 – 200 kpc (see Section 2.2.4), as well as initial velocity perturbations on the same scale. In the strong initial field simulations the resulting Alfvén Mach number is less than one at large radii, which means that the magnetic fields can readily exert force on the plasma via magnetic tension in that region of the cluster. Since the initial field configuration was not designed to be initially force-free (i.e., $(\nabla \times \mathbf{B}) \times \mathbf{B} = 0$), it is likely that the magnetic field is exerting force on the plasma and transferring its energy into fluid motion. In the weak initial field run the gas velocity is highly super-Alfvénic

at large radii at all times, which means that it is difficult for this transfer of energy to occur in that region of the cluster. Conclusive evidence for this is phenomenon is challenging to obtain because fluid motion is observed in all of the simulations at large radii (see the top panel of Figure 8) at late times. This is difficult to disentangle from kinetic energy deposited by the AGN jet, and further analysis is required.

4.3. On the impact of the AGN jet

Figure 14 shows the location of tracer fluid from the AGN as a function of radius and polar angle, both at a specific time and averaged over a range of time. The instantaneous and time-averaged results are broadly consistent with each other and show where the AGN plasma has been mixed in with the ambient medium. In the central region of the cluster ($r \lesssim 10$ kpc) we see that this tracer fluid is relatively isotropically distributed, but there is relatively little of it – most of the jet material ends up at large cluster radii. At those radii the tracer fluid in the stronger initial field cases is constrained to be in the polar regions of the cluster (i.e., along the z-axis of the simulation, which is the jet launching axis), and out to $\simeq 300$ kpc in both cases. The jet material ends up at quite large radii, consistent with it being launched with a high entropy and then buoyantly rising for some distance.

The **WeakMag** and **Hydro** simulations have similar behavior at small radii, but the tracer fluid does not reach as far from the centre as the **Fiducial** and **WeakCool** cases. The difference between the different initial field strengths are striking. In both cases, the jets are magnetized at identical fractional levels although the total amount of magnetic energy is scaled to the AGN power, which differs by a factor of $\simeq 6$. However, the behavior of the **WeakMag** run is quite similar to the **Hydro** run. This suggests that the relatively strong magnetic field in the ambient medium ($\sim 1 \mu\text{G}$ in the strong field case compared to $0.01 \mu\text{G}$ in the weak field case) suppresses mixing of the jet material and thus facilitates its buoyant rise to large radii. This is plausible, because even though the magnetic field is globally weak at large radii (with $\beta \simeq 10^3$ at large radii in the strong field case) magnetic tension can still be a significant factor on small scales. However, further analysis is required to disentangle the causalities given the differences in AGN power over time.

4.4. On the origin and evolution of cold gas

While all of the simulations have cold gas in them, the simulations with stronger magnetic fields have cold gas that goes out to significantly larger radii. Figure 6 shows that significant amounts of cold gas can be seen

out to $\simeq 80$ kpc in the case with the strongest cooling and out to $\simeq 40$ kpc in the weaker cooling case. We emphasize that our simulations are run with homogeneous and constant metallicity and that this assumption in the strong cooling runs does not hold in reality, as metallicity in the Perseus cluster is observed to reach values below $\sim 0.5 Z_{\odot}$ for radii larger than ~ 50 kpc (Sanders & Fabian 2007). Assuming Solar metallicity everywhere in the simulated box likely results in overestimated cooling at larger radii. In the weak initial field and hydrodynamical case (both with strong cooling) cold gas is largely constrained to be within a rotating disk with a radius of $\simeq 5 - 6$ kpc. The bottom panel of Figure 3 suggests that the *total amount* of cold gas is also impacted by the magnetic fields – the high magnetic field run with strong cooling has $3 - 4\times$ more cold gas than the weak field run with the same level of cooling, and $8 - 10\times$ the cold gas seen in the hydrodynamical run, from $T = 1.5 - 2.5$ Gyr. This run also has a factor of a few more cold gas than the equivalent run with weaker cooling. From these results we infer that magnetic fields both promote the formation of cold gas and allow it to be much more widely distributed in the cluster than in cases with negligible or absent fields. Morphologically, simulations with strong fields tend to develop cold “filaments,” possibly aligned with the local magnetic field structure. In Fournier et al. (2024) this behavior is studied in some detail, and we will continue to investigate this topic in a following paper.

4.5. Computational challenges and solutions

While the ATHENAPK code is highly performant, highly scalable, and based on a codebase that is extensively used for massively parallel simulations on GPU-based computers (i.e., the Parthenon framework; Grete et al. 2023), moving to a completely new computing platform typically exposes new challenges. This is particularly true when moving to a platform such as the Frontier exascale supercomputer (Atchley et al. 2023) at the Oak Ridge Leadership Computing Facility (OLCF), which at the time we began to run our calculations on it in mid-2023 was the largest supercomputer in the world⁷. Frontier, unlike most other large GPU-based supercomputers, uses the AMD “Instinct” MI250X GPUs rather than NVIDIA GPUs, has an HPE Slingshot interconnect, and has a site-wide 700 PB Lustre filesystem (“Orion”) that has its own large compute cluster to manage I/O and metadata for Frontier and OLCF’s other supercomputers. This means that, in addition to

running ATHENAPK simulations at a scale more than an order of magnitude larger than on previous systems, we were doing so with very new (and thus relatively untested) computing, networking, and file storage hardware and their associated hardware drivers, compilers, MPI and parallel I/O libraries, and other related software. This resulted in several specific challenges that had to be solved, which we detail below; in addition, we direct the interested reader to Holmen et al. (2024) for a more detailed analysis of performance variability of ATHENAPK on Frontier.

The most notable challenge we ran into was related to the Lustre file system. When we began this project ATHENAPK used the HDF5 library (Folk et al. 2011), which uses MPI-IO for parallel reading and writing of files (Thakur et al. 1999). While this gave perfectly acceptable results on smaller systems (such as Frontier’s $\simeq 200$ petaflop predecessor, Summit) we found that HDF5+MPI-IO was both extremely slow on Frontier (taking more than half an hour to write an output file using the default filesystem and MPI-IO configuration) and very unstable – simulations would crash with very little feedback or silently stall, wasting allocation time⁸. After extensive experimentation with environmental variables we found that disabling collective buffering, disabling the “self extending layout” and setting a fixed stripe size (to $2/3$ of the maximum OSTs) resulted in acceptable (though not ideal) performance, i.e., writing an output file in $\mathcal{O}(3)$ minutes, in cases where the write was successful and not stalling. One key issue of our IO approach remained though: writing to a single file. To mitigate this (in the long run) we added support for the OpenPMD file format (Huebl et al. 2015), which can make use of the ADIOS2 scalable I/O framework (Poeschel et al. 2022). ADIOS2 implements a streaming data pipeline methodology that effectively decouples the simulation code itself from the I/O subsystem, allowing much greater flexibility than HDF5+MPI-IO. Furthermore, the ADIOS2 framework is well-matched to the design of modern supercomputer file systems. As a consequence of this change we removed I/O performance as a bottleneck in future simulations.

In an attempt to reduce the volume of data output and the associated analysis burden, we added support for using the ASCENT in-situ visualization library (Larsen et al. 2022) to ATHENAPK, but encountered multiple issues with performance and correctness. Since AS-

⁷ see <https://top500.org/lists/top500/2023/11/>

⁸ As a temporary workaround to silent stalls in IO wasting allocation time, we added logic to our job scripts to monitor activity in `STDOUT`. If nothing was written to `STDOUT` for a minute, we made the job script terminate itself.

CENT internally uses HDF5, using ASCENT to produce slices of our simulations as they were running created an I/O bottleneck that we were unable to resolve. Additionally, support for ghost zones is inconsistent internally throughout ASCENT, so we were unable to generate correct histograms or spherically-averaged profiles using this library. We also found that performance of several ASCENT components were significantly worse on AMD GPUs as compared to NVIDIA GPUs, but we were unable to find a workaround for these issues. This led to the addition of calculating histograms in-situ in PARTHENON itself.

4.6. *Limitations*

As with all numerical simulations, the work presented in this paper (and in the following papers in this series) have limitations. The most important limitations are discussed in the following subsections:

4.6.1. *Missing Energy Sources*

Aside from the AGN at the cluster center and the volumetric thermal feedback from the central galaxy’s stellar population, there are no additional sources of energy injection in these simulations. That means that we are missing several potential sources of energy that might stimulate bulk motion and turbulence, and ultimately heat the intracluster medium. These missing sources originate from the hierarchical growth of cosmic structure. That is, we are missing the potential impact of recent cluster mergers (e.g., shocks and “sloshing” in the ICM), accretion of material (including galaxies and filamentary plasma) from the cosmic web, motions of non-central galaxies in the intracluster medium, and more generally, the motion of any massive substructure in the cluster. While these dynamical energy sources significantly contribute to a galaxy cluster’s overall energy budget over its lifetime, it is unlikely that any of them dominate the heating rate in a cluster’s innermost regions (i.e., in the region where we focus our efforts). For example, [Fielding et al. \(2020\)](#) compare both cosmological and idealized simulations of Milky Way-mass galaxies and find results that are similar at small fractions of the virial radii, but differ significantly at larger radii, indicating that dynamical heating is less important than feedback heating at small radii. One would expect this trend to continue at larger halo mass scales, with deeper gravitational potential wells constraining the relevance of idealized simulations such as ours to even smaller fractions of the virial radius.

4.6.2. *Plasma Physics*

We neglect the impact of plasma physics beyond the assumptions built into the equations of ideal magnetohy-

drodynamics (MHD). We do not include cosmic ray populations, which could potentially be a significant component of the ICM energy budget in certain subvolumes (such as AGN jet-driven bubbles) as well as valuable sources of observational information from, e.g., radio emission from cosmic ray electrons (see, e.g., [Ruszkowski & Pfrommer 2023](#), for a recent review). We are also missing the impact of non-ideal MHD effects relating to the weak collisionality of the ICM plasma, such as anisotropic viscosity, conduction, and the local generation of magnetic fields. The consequences of this physics have been extensively studied both analytically and numerically (see, e.g., [Schekochihin et al. 2009](#); [Kunz et al. 2012](#); [ZuHone et al. 2015](#); [St-Onge & Kunz 2018](#); [Squire et al. 2023](#); [Zhou et al. 2024](#)). Inclusion of additional plasma physics is a clear avenue for future work. We are also explicitly ignoring both special and general relativity when modeling the impact of AGN jet feedback in group and cluster environments. This is a reasonable approximation because the spatial and temporal scales that we are modeling are orders of magnitude larger than those relevant to, e.g., general relativistic MHD simulations of black hole accretion and jet launching (see, e.g., [Liska et al. 2020](#); [Kaaz et al. 2023](#)), and by the time the launched jets approach the scales that we are modeling they are weakly relativistic at most (i.e., $\frac{v}{c} \ll 1$).

4.6.3. *Stellar Feedback*

The algorithms that we use to approximate star formation and supernova mass and energy feedback in the central cluster galaxy (Sec. 2.2.11) are relatively simple, and in particular are volumetric rather than particle-based in nature. In addition, feedback that approximates Type II supernovae originating from cold, dense gas in the halo center is approximated as instantaneous feedback rather than including a physically-appropriate delay. We include feedback using this volumetric method because both theory and previous simulations have shown that it is potentially important for the self-regulation of the circumgalactic media in massive galaxies (see, e.g., [Voit et al. 2020](#); [Prasad et al. 2020](#)). Still stellar feedback is globally sub-dominant. It is unclear if having a more granular stellar feedback algorithm would make a significant difference at the spatial and mass resolutions we are considering (in contrast to, e.g., at the dwarf or Milky Way-galaxy scale). This is also an area of potential future study.

4.7. *Future papers in this series*

This paper is the first in a series of publications presenting the results from our simulation campaign, and presents a high-level overview of a subset of the simulations. In the following papers we will perform detailed

analyses of specific aspects of the simulations and examine a broader range of galaxy groups and clusters than is presented in this paper. Specifically, we plan to do the following:

We will examine the mechanisms by which the magnetized AGN jets inject energy and drive turbulence in the intracluster medium, and will examine the detailed properties of that turbulence using the energy transfer analysis tools that we have developed (Grete et al. 2017). This extends previous work done by this collaboration on driven MHD turbulence (e.g., Grete et al. 2021, 2023) into more physically-realistic environments.

We will create synthetic observations of the H α and X-ray-emitting plasma in our simulated clusters and compare this to galaxy cluster observations that are probing the dynamical state of local clusters (e.g., Li et al. 2020; de Vries et al. 2023). In particular, we intend to examine the relationship between turbulent power spectra, line-of-sight velocity structure functions, X-ray surface brightness fluctuations, and potential systematic differences between the behavior seen at the resolution of the simulations themselves vs. what can be discerned via measurements made with current observatories.

We will use the full simulation suite, which includes galaxy groups with significantly different entropy profiles (motivated by Prasad et al. 2020, 2022) and galaxy clusters spanning the mass range $10^{14} - 10^{15} M_{\odot}$ to examine the self-regulating behavior of magnetized AGN in this range of environments using a uniform set of physics and numerical methods.

We will compare subvolumes extracted from our calculations with more idealized numerical experiments in order to understand systematic differences between them, and thus address challenges in connecting both to observations. Our intent is to initially focus on comparisons with setups of hydrodynamic and magnetohydrodynamic turbulence in stratified media and the generation of multiphase structures (e.g., Ji et al. 2018; Mohapatra et al. 2022; Wibking et al. 2024), but ultimately we will extend these comparisons to a broader range of phenomena.

It is also our intention to make this simulation data publicly available within a reasonable time period. The primary challenge relates to data volume – the raw data produced by our simulation campaign exceeds 4 petabytes, and it will take time to process this data to reduce its overall volume, to generate metadata, and to archive it in a place where it can be acquired. We anticipate that this will require: (1) excising the scientifically interesting subvolumes of simulations from the full-scale calculations; (2) reducing the overall precision of the datasets produced (likely by using a lossy data compression

method); (3) extensively documenting these steps as well as all simulation parameter files, codes, and output files; and (4) working with support staff at the relevant national computing centers to ensure that these datasets are available in a findable and searchable way.

5. CONCLUSIONS AND OUTLOOK

This is the first paper in a series presenting results on the first exascale simulations examining the self-regulation of idealized galaxy clusters with magnetized jets. The key results from this work are as follows:

1. The idealized exascale MHD cluster simulations in this study self-regulate. For the duration of the simulations the cluster core maintains a roughly constant thermodynamic state including significant amounts of cold gas ($M_{\text{cold}} \sim 10^{10} M_{\odot}$). The AGN injects energy at variable rates of $\simeq 10^{44} - 10^{45}$ erg/s, with no discernible on/off duty cycle as is often seen in comparable hydrodynamic simulations. This is in agreement with radio observations of massive galaxy clusters (Sabater et al. 2019). Despite having no precession of the AGN jet we observe variability in the jets' alignment as well as episodic behavior due to the interaction of the jets with cold gas in the cluster center.
2. Cold gas filaments are not monolithic; rather, they have complex structures. The interaction of the jet with the cold gas leads to appreciable deflection of the jets, as discussed in detail in Fournier et al. (2024). Our simulations also show that AGN jets form large cavities in the ICM, some of which are off-axis (deflected away from jet axis) due to this interaction.
3. Magnetic fields significantly impact the formation and distribution of cold gas. Simulations initialized with stronger magnetic fields ($B = 1 \mu\text{G}$) show enhanced cold gas formation out to much larger radii ($r \sim 100$ kpc) compared to hydro simulations or those initialized with weak magnetic fields ($B = 0.001 \mu\text{G}$) where cold gas is typically seen within $r < 20$ kpc. The total amount of cold gas that is produced depends on both the cooling function (i.e., the assumed ICM metallicity) and the initial magnetic field strength. It is comparable between hydrodynamic simulation, the one with weak magnetic fields ($B = 0.001 \mu\text{G}$), and the simulation with strong magnetic fields ($B = 1 \mu\text{G}$) but a lower-metallicity ($0.3 Z_{\odot}$) cooling function.
4. The AGN jet drives the amplification of magnetic fields in the cluster cores. Magnetic field amplification is locally fast (more than $100\times$ in less than

100 Myr on the smallest scales) compared to global time scales (i.e., the sound-crossing time scale of the cluster core).

5. Both the kinetic and magnetic energy power spectra of turbulence in the cluster core grows over the first ~ 1 Gyr of AGN jet activity and ultimately achieves a roughly steady state. Moreover, the fluctuations in the power spectra amplitude and slope are linked to the AGN jet energy injection rate.
6. The AGN feedback ‘sphere of influence’ is limited to the cluster core in all simulations (i.e., it is contained within a cluster-centric radius of $\simeq 100$ kpc). Within the ‘sphere of influence’ ($r \sim 100$ kpc) AGN drive turbulence that leads to magnetic field amplification and the formation of filaments of cold gas. The entropy profiles of the ICM show the impact of the cooling and feedback cycle within the cluster out to $\simeq 100$ kpc. Simulations with lower metallicity and weaker magnetic fields tend to have more radially-concentrated cold gas and magnetic fields.
7. A passive tracer fluid injected with the AGN shows that the effect of the AGN on the ICM is confined to the polar regions of the cluster at relatively large radii ($\gtrsim 10$ kpc). The jet-polluted material in the more highly magnetized simulations tend to stay in the polar regions and can be found at larger radii (out to $\simeq 300$ kpc) compared to simulations with weak or no magnetic fields, which have a more uniform (albeit still polar) and centrally-concentrated ($\lesssim 120$ kpc) distribution in their affected regions. In contrast, the turbulence driven by the AGN is volume-filling within the cluster core, which demonstrates that the impact of the AGN can be felt outside of the region that is directly mixed with the jet ejecta.

In the following papers in this series we will examine the mechanisms by which the magnetized AGN jets inject energy and drive turbulence in the intra-cluster medium, as well as show the detailed properties of that turbulence (including energy transfer). More-

over, we will make detailed comparisons with multi-wavelength observations. Finally, we will examine the self-regulating behavior of magnetized AGN in galaxy group as well as in clusters of a range of masses and compare subvolumes extracted from our calculations with more idealized setups of, e.g., turbulence in stratified media.

1 The authors thank Greg Bryan, Hui Li, Yuan Li, Ri-
 2 carda Beckmann, and Rainer Weinberger for insight-
 3 ful discussions and the Oak Ridge Leadership Com-
 4 puting Facility support staff, in particular John Hol-
 5 men, for incredibly valuable support at all stages of
 6 the INCITE project that resulted in this and follow-
 7 ing publications. BDW thanks Michael Zingale for use-
 8 ful discussions of performance, scaling, and bugs on
 9 FRONTIER. BWO acknowledges support from NSF
 10 grants #1908109 and #2106575, NASA ATP grants
 11 NNX15AP39G and 80NSSC18K1105, and NASA TCAN
 12 grant 80NSSC21K1053. BWO also thanks the Los
 13 Alamos National Laboratory Center for Nonlinear Stud-
 14 ies for support via the Ulam Sabbatical Fellowship.
 15 This research used resources of the Oak Ridge Lead-
 16 ership Computing Facility at the Oak Ridge National
 17 Laboratory, which is supported by the Office of Science
 18 of the U.S. Department of Energy under Contract No.
 19 DE-AC05-00OR22725. These resources were provided
 20 by as part of the DOE INCITE Leadership Computing
 21 Program under allocation AST-146 (PI: Brian O’Shea).
 22 MF and MB acknowledge funding by the Deutsche
 23 Forschungsgemeinschaft (DFG, German Research Founda-
 24 tion) under Germany’s Excellence Strategy – EXC
 25 2121 “Quantum Universe” – 390833306. DP is sup-
 26 ported by the Royal Society through UKRI grant RF-
 27 ERE-210263 (PI: Freeke van de Voort). All simu-
 28 lations were performed using the public MHD code
 29 [ATHENAPK](#), which makes use of the [KOKKOS](#) library
 30 ([Trott et al. 2022](#)) and the [PARTHENON](#) adaptive mesh
 31 refinement framework ([Grete et al. 2023](#)). All data anal-
 32 ysis was performed with [YT](#) ([Turk et al. 2011, 2024](#)),
 33 [MATPLOTLIB](#) ([Hunter 2007](#)), and [NUMPY](#) ([Harris et al.](#)
 34 [2020](#)). We thank their authors for making these software
 35 and packages publicly available.

REFERENCES

- Atchley, S., Zimmer, C., Lange, J., et al. 2023, in Proceedings of the International Conference for High Performance Computing, Networking, Storage and Analysis, SC ’23 (New York, NY, USA: Association for Computing Machinery), doi: [10.1145/3581784.3607089](https://doi.org/10.1145/3581784.3607089)
- Beattie, J. R., Federrath, C., Klessen, R. S., Cielo, S., & Bhattacharjee, A. 2024, arXiv e-prints, arXiv:2405.16626, doi: [10.48550/arXiv.2405.16626](https://doi.org/10.48550/arXiv.2405.16626)

- Beckmann, R. S., Dubois, Y., Guillard, P., et al. 2019, *Astronomy & Astrophysics*, 631, A60, doi: [10.1051/0004-6361/201936188](https://doi.org/10.1051/0004-6361/201936188)
- Biava, N., Brienza, M., Bonafede, A., et al. 2021, *A&A*, 650, A170, doi: [10.1051/0004-6361/202040063](https://doi.org/10.1051/0004-6361/202040063)
- Birzan, L., Rafferty, D. A., McNamara, B. R., Wise, M. W., & Nulsen, P. E. J. 2004, *ApJ*, 607, 800, doi: [10.1086/383519](https://doi.org/10.1086/383519)
- Brandenburg, A., & Subramanian, K. 2005, *Physics Reports*, 417, 1, doi: [10.1016/j.physrep.2005.06.005](https://doi.org/10.1016/j.physrep.2005.06.005)
- Cavagnolo, K. W., Donahue, M., Voit, G. M., & Sun, M. 2008, *ApJL*, 683, L107, doi: [10.1086/591665](https://doi.org/10.1086/591665)
- Cavagnolo, K. W., Donahue, M., Voit, G. M., & Sun, M. 2009, *ApJS*, 182, 12, doi: [10.1088/0067-0049/182/1/12](https://doi.org/10.1088/0067-0049/182/1/12)
- Cavagnolo, K. W., McNamara, B. R., Nulsen, P. E. J., et al. 2010, *ApJ*, 720, 1066, doi: [10.1088/0004-637X/720/2/1066](https://doi.org/10.1088/0004-637X/720/2/1066)
- Churazov, E., Brügggen, M., Kaiser, C. R., Böhringer, H., & Forman, W. 2001, *ApJ*, 554, 261, doi: [10.1086/321357](https://doi.org/10.1086/321357)
- de Vries, M., Mantz, A. B., Allen, S. W., et al. 2023, *MNRAS*, 518, 2954, doi: [10.1093/mnras/stac3285](https://doi.org/10.1093/mnras/stac3285)
- Dedner, A., Kemm, F., Kröner, D., et al. 2002, *Journal of Computational Physics*, 175, 645, doi: [10.1006/jcph.2001.6961](https://doi.org/10.1006/jcph.2001.6961)
- Donahue, M., & Voit, G. M. 2022, *PhR*, 973, 1, doi: [10.1016/j.physrep.2022.04.005](https://doi.org/10.1016/j.physrep.2022.04.005)
- Edge, A. C. 2001, *MNRAS*, 328, 762, doi: [10.1046/j.1365-8711.2001.04802.x](https://doi.org/10.1046/j.1365-8711.2001.04802.x)
- Ehlert, K., Weinberger, R., Pfrommer, C., Pakmor, R., & Springel, V. 2023, *MNRAS*, 518, 4622, doi: [10.1093/mnras/stac2860](https://doi.org/10.1093/mnras/stac2860)
- Fabian, A. C. 1994, *ARA&A*, 32, 277, doi: [10.1146/annurev.aa.32.090194.001425](https://doi.org/10.1146/annurev.aa.32.090194.001425)
- Fabian, A. C., Nulsen, P. E. J., & Canizares, C. R. 1984, *Nature*, 310, 733, doi: [10.1038/310733a0](https://doi.org/10.1038/310733a0)
- Federrath, C., Klessen, R. S., Iapichino, L., & Beattie, J. R. 2021, *Nature Astronomy*, 5, 365, doi: [10.1038/s41550-020-01282-z](https://doi.org/10.1038/s41550-020-01282-z)
- Field, G. B. 1965, *ApJ*, 142, 531, doi: [10.1086/148317](https://doi.org/10.1086/148317)
- Fielding, D. B., Tonnesen, S., DeFelippis, D., et al. 2020, *ApJ*, 903, 32, doi: [10.3847/1538-4357/abbc6d](https://doi.org/10.3847/1538-4357/abbc6d)
- Folk, M., Heber, G., Koziol, Q., Pourmal, E., & Robinson, D. 2011, in *Proceedings of the EDBT/ICDT 2011 Workshop on Array Databases*, AD '11 (New York, NY, USA: Association for Computing Machinery), 36–47, doi: [10.1145/1966895.1966900](https://doi.org/10.1145/1966895.1966900)
- Fournier, M., Grete, P., Brügggen, M., Glines, F. W., & O'Shea, B. W. 2024, *A&A*, 691, A239, doi: [10.1051/0004-6361/202451031](https://doi.org/10.1051/0004-6361/202451031)
- Ganguly, S., Li, Y., Olivares, V., et al. 2023, *The Nature of the Motions of Multiphase Filaments in the Centers of Galaxy Clusters*. <https://arxiv.org/abs/2304.09879>
- Gaspari, M., Ruszkowski, M., & Oh, S. P. 2013, *MNRAS*, 432, 3401, doi: [10.1093/mnras/stt692](https://doi.org/10.1093/mnras/stt692)
- Gaspari, M., Ruszkowski, M., & Sharma, P. 2012, *ApJ*, 746, 94, doi: [10.1088/0004-637X/746/1/94](https://doi.org/10.1088/0004-637X/746/1/94)
- Gingras, M.-J., Coil, A. L., McNamara, B. R., et al. 2024, *ApJ*, 977, 159, doi: [10.3847/1538-4357/ad822a](https://doi.org/10.3847/1538-4357/ad822a)
- Grete, P., O'Shea, B. W., & Beckwith, K. 2021, *ApJ*, 909, 148, doi: [10.3847/1538-4357/abdd22](https://doi.org/10.3847/1538-4357/abdd22)
- . 2023, *ApJL*, 942, L34, doi: [10.3847/2041-8213/acaee7](https://doi.org/10.3847/2041-8213/acaee7)
- Grete, P., O'Shea, B. W., Beckwith, K., Schmidt, W., & Christlieb, A. 2017, *Physics of Plasmas*, 24, 092311, doi: [10.1063/1.4990613](https://doi.org/10.1063/1.4990613)
- Grete, P., Dolence, J. C., Miller, J. M., et al. 2023, *The International Journal of High Performance Computing Applications*, 37, 465, doi: [10.1177/10943420221143775](https://doi.org/10.1177/10943420221143775)
- Guo, M., Stone, J. M., Quataert, E., & Kim, C.-G. 2024, *The Astrophysical Journal*, 973, 141, doi: [10.3847/1538-4357/ad5fe7](https://doi.org/10.3847/1538-4357/ad5fe7)
- Harris, C. R., Millman, K. J., van der Walt, S. J., et al. 2020, *Nature*, 585, 357, doi: [10.1038/s41586-020-2649-2](https://doi.org/10.1038/s41586-020-2649-2)
- Holmen, J. K., Grete, P., & Melesse Vergara, V. G. 2024, *Concurrency and Computation: Practice and Experience*, 36, e8069, doi: <https://doi.org/10.1002/cpe.8069>
- Hudson, D. S., Mittal, R., Reiprich, T. H., et al. 2010, *A&A*, 513, A37, doi: [10.1051/0004-6361/200912377](https://doi.org/10.1051/0004-6361/200912377)
- Huebl, A., Lehe, R., Kuschel, S., et al. 2015, *The openPMD Standard*, doi: [10.11578/dc.20220810.25](https://doi.org/10.11578/dc.20220810.25)
- Hunter, J. D. 2007, *Computing in Science and Engineering*, 9, 90, doi: [10.1109/MCSE.2007.55](https://doi.org/10.1109/MCSE.2007.55)
- Ji, S., Oh, S. P., & McCourt, M. 2018, *MNRAS*, 476, 852, doi: [10.1093/mnras/sty293](https://doi.org/10.1093/mnras/sty293)
- Kaaz, N., Murguia-Berthier, A., Chatterjee, K., Liska, M. T. P., & A. 2023, *ApJ*, 950, 31, doi: [10.3847/1538-4357/acc7a1](https://doi.org/10.3847/1538-4357/acc7a1)
- Kunz, M. W., Bogdanović, T., Reynolds, C. S., & Stone, J. M. 2012, *ApJ*, 754, 122, doi: [10.1088/0004-637X/754/2/122](https://doi.org/10.1088/0004-637X/754/2/122)
- Larsen, M., Brugger, E., Childs, H., & Harrison, C. 2022, in *In Situ Visualization For Computational Science* (Cham, Switzerland: Mathematics and Visualization book series from Springer Publishing), 255 – 279
- Li, Y., & Bryan, G. L. 2014, *The Astrophysical Journal*, 789, 54, doi: [10.1088/0004-637x/789/1/54](https://doi.org/10.1088/0004-637x/789/1/54)
- Li, Y., Bryan, G. L., Ruszkowski, M., et al. 2015, *ApJ*, 811, 73, doi: [10.1088/0004-637X/811/2/73](https://doi.org/10.1088/0004-637X/811/2/73)
- Li, Y., Gendron-Marsolais, M.-L., Zhuravleva, I., et al. 2020, *ApJL*, 889, L1, doi: [10.3847/2041-8213/ab65c7](https://doi.org/10.3847/2041-8213/ab65c7)

- Liska, M., Tchekhovskoy, A., & Quataert, E. 2020, MNRAS, 494, 3656, doi: [10.1093/mnras/staa955](https://doi.org/10.1093/mnras/staa955)
- Mathews, W. G., Faltenbacher, A., & Brighenti, F. 2006, ApJ, 638, 659, doi: [10.1086/499119](https://doi.org/10.1086/499119)
- McCourt, M., Sharma, P., Quataert, E., & Parrish, I. J. 2012, MNRAS, 419, 3319, doi: [10.1111/j.1365-2966.2011.19972.x](https://doi.org/10.1111/j.1365-2966.2011.19972.x)
- McDonald, M., Allen, S. W., Hlavacek-Larrondo, J., et al. 2019, ApJ, 870, 85, doi: [10.3847/1538-4357/aaf394](https://doi.org/10.3847/1538-4357/aaf394)
- McNamara, B. R., Russell, H. R., Nulsen, P. E. J., et al. 2014, ApJ, 785, 44, doi: [10.1088/0004-637X/785/1/44](https://doi.org/10.1088/0004-637X/785/1/44)
- Meece, G. R., Voit, G. M., & O'Shea, B. W. 2017, ApJ, 841, 133, doi: [10.3847/1538-4357/aa6fb1](https://doi.org/10.3847/1538-4357/aa6fb1)
- Miyoshi, T., & Kusano, K. 2005, Journal of Computational Physics, 208, 315, doi: [10.1016/j.jcp.2005.02.017](https://doi.org/10.1016/j.jcp.2005.02.017)
- Mohapatra, R., Federrath, C., & Sharma, P. 2022, MNRAS, 514, 3139, doi: [10.1093/mnras/stac1610](https://doi.org/10.1093/mnras/stac1610)
- Mohapatra, R., Sharma, P., Federrath, C., & Quataert, E. 2023, MNRAS, 525, 3831, doi: [10.1093/mnras/stad2574](https://doi.org/10.1093/mnras/stad2574)
- Naab, T., & Ostriker, J. P. 2017, ARA&A, 55, 59, doi: [10.1146/annurev-astro-081913-040019](https://doi.org/10.1146/annurev-astro-081913-040019)
- Navarro, J. F., Frenk, C. S., & White, S. D. M. 1997, ApJ, 490, 493, doi: [10.1086/304888](https://doi.org/10.1086/304888)
- Nelson, D., Pillepich, A., Ayromlou, M., et al. 2024, A&A, 686, A157, doi: [10.1051/0004-6361/202348608](https://doi.org/10.1051/0004-6361/202348608)
- Nobels, F. S. J., Schaye, J., Schaller, M., Bahé, Y. M., & Chaikin, E. 2022, MNRAS, 515, 4838, doi: [10.1093/mnras/stac2061](https://doi.org/10.1093/mnras/stac2061)
- O'Dea, C. P., Baum, S. A., Privon, G., et al. 2008, ApJ, 681, 1035, doi: [10.1086/588212](https://doi.org/10.1086/588212)
- Olivares, V., Salome, P., Combes, F., et al. 2019, A&A, 631, A22, doi: [10.1051/0004-6361/201935350](https://doi.org/10.1051/0004-6361/201935350)
- Oosterloo, T., Morganti, R., & Murthy, S. 2024, Nature Astronomy, 8, 256, doi: [10.1038/s41550-023-02138-y](https://doi.org/10.1038/s41550-023-02138-y)
- O'Shea, B. W., Nagamine, K., Springel, V., Hernquist, L., & Norman, M. L. 2005, ApJS, 160, 1, doi: [10.1086/432645](https://doi.org/10.1086/432645)
- Panagoulia, E. K., Fabian, A. C., Sanders, J. S., & Hlavacek-Larrondo, J. 2014, MNRAS, 444, 1236, doi: [10.1093/mnras/stu1499](https://doi.org/10.1093/mnras/stu1499)
- Pellissier, A., Hahn, O., & Ferrari, C. 2023, MNRAS, 522, 721, doi: [10.1093/mnras/stad888](https://doi.org/10.1093/mnras/stad888)
- Peterson, J. R., Kahn, S. M., Paerels, F. B. S., et al. 2003, ApJ, 590, 207, doi: [10.1086/374830](https://doi.org/10.1086/374830)
- Pizzolato, F., & Soker, N. 2005, ApJ, 632, 821, doi: [10.1086/444344](https://doi.org/10.1086/444344)
- Poeschel, F., E, J., Godoy, W. F., et al. 2022, in Driving Scientific and Engineering Discoveries Through the Integration of Experiment, Big Data, and Modeling and Simulation, ed. J. Nichols, A. B. Maccabe, J. Nutaro, S. Pophale, P. Devineni, T. Ahearn, & B. Verastegui (Cham: Springer International Publishing), 99–118
- Prasad, D., Sharma, P., & Babul, A. 2015, ApJ, 811, 108, doi: [10.1088/0004-637X/811/2/108](https://doi.org/10.1088/0004-637X/811/2/108)
- Prasad, D., Voit, G. M., & O'Shea, B. W. 2022, ApJ, 932, 18, doi: [10.3847/1538-4357/ac69ee](https://doi.org/10.3847/1538-4357/ac69ee)
- Prasad, D., Voit, G. M., O'Shea, B. W., & Glines, F. 2020, ApJ, 905, 50, doi: [10.3847/1538-4357/abc33c](https://doi.org/10.3847/1538-4357/abc33c)
- Prunier, M., Hlavacek-Larrondo, J., Pillepich, A., Lehle, K., & Nelson, D. 2024, X-ray cavities in TNG-Cluster: AGN phenomena in the full cosmological context. <https://arxiv.org/abs/2410.21366>
- Qiu, Y., Bogdanović, T., Li, Y., Park, K., & Wise, J. H. 2019, The Astrophysical Journal, 877, 47, doi: [10.3847/1538-4357/ab18fd](https://doi.org/10.3847/1538-4357/ab18fd)
- Rafferty, D. A., McNamara, B. R., & Nulsen, P. E. J. 2008, ApJ, 687, 899, doi: [10.1086/591240](https://doi.org/10.1086/591240)
- Rafferty, D. A., McNamara, B. R., Nulsen, P. E. J., & Wise, M. W. 2006, ApJ, 652, 216, doi: [10.1086/507672](https://doi.org/10.1086/507672)
- Riffel, R. A., Storchi-Bergmann, T., Zakamska, N. L., & Riffel, R. 2020, MNRAS, 496, 4857, doi: [10.1093/mnras/staa1922](https://doi.org/10.1093/mnras/staa1922)
- Rincon, F. 2019, Journal of Plasma Physics, 85, 205850401, doi: [10.1017/S0022377819000539](https://doi.org/10.1017/S0022377819000539)
- Ruszkowski, M., & Pfrommer, C. 2023, A&A Rv, 31, 4, doi: [10.1007/s00159-023-00149-2](https://doi.org/10.1007/s00159-023-00149-2)
- Sabater, J., Best, P. N., Hardcastle, M. J., et al. 2019, A&A, 622, A17, doi: [10.1051/0004-6361/201833883](https://doi.org/10.1051/0004-6361/201833883)
- Salomé, P., Combes, F., Edge, A. C., et al. 2006, A&A, 454, 437, doi: [10.1051/0004-6361:20054745](https://doi.org/10.1051/0004-6361:20054745)
- Sanders, J. S., & Fabian, A. C. 2007, Monthly Notices of the Royal Astronomical Society, 381, 1381–1399, doi: [10.1111/j.1365-2966.2007.12347.x](https://doi.org/10.1111/j.1365-2966.2007.12347.x)
- Schaye, J., Kugel, R., Schaller, M., et al. 2023, MNRAS, 526, 4978, doi: [10.1093/mnras/stad2419](https://doi.org/10.1093/mnras/stad2419)
- Schekochihin, A. A., Cowley, S. C., Dorland, W., et al. 2009, ApJS, 182, 310, doi: [10.1088/0067-0049/182/1/310](https://doi.org/10.1088/0067-0049/182/1/310)
- Schure, K. M., Kosenko, D., Kaastra, J. S., Keppens, R., & Vink, J. 2009, Astronomy & Astrophysics, 508, 751, doi: [10.1051/0004-6361/200912495](https://doi.org/10.1051/0004-6361/200912495)
- Shimwell, T. W., Hardcastle, M. J., Tasse, C., et al. 2022, A&A, 659, A1, doi: [10.1051/0004-6361/202142484](https://doi.org/10.1051/0004-6361/202142484)
- Simionescu, A., Allen, S. W., Mantz, A., et al. 2011, Science, 331, 1576, doi: [10.1126/science.1200331](https://doi.org/10.1126/science.1200331)

- Squire, J., Kunz, M. W., Arzamasskiy, L., et al. 2023, *Journal of Plasma Physics*, 89, 905890417, doi: [10.1017/S0022377823000727](https://doi.org/10.1017/S0022377823000727)
- St-Onge, D. A., & Kunz, M. W. 2018, *ApJL*, 863, L25, doi: [10.3847/2041-8213/aad638](https://doi.org/10.3847/2041-8213/aad638)
- Stone, J. M., Tomida, K., White, C. J., & Felker, K. G. 2020, *The Astrophysical Journal Supplement Series*, 249, 4, doi: [10.3847/1538-4365/ab929b](https://doi.org/10.3847/1538-4365/ab929b)
- Sun, M., Voit, G. M., Donahue, M., et al. 2009, *ApJ*, 693, 1142, doi: [10.1088/0004-637X/693/2/1142](https://doi.org/10.1088/0004-637X/693/2/1142)
- Thakur, R., Gropp, W., & Lusk, E. 1999, in *Proceedings of the Sixth Workshop on I/O in Parallel and Distributed Systems*, IOPADS '99 (New York, NY, USA: Association for Computing Machinery), 23–32, doi: [10.1145/301816.301826](https://doi.org/10.1145/301816.301826)
- Townsend, R. H. D. 2009, *The Astrophysical Journal Supplement Series*, 181, 391, doi: [10.1088/0067-0049/181/2/391](https://doi.org/10.1088/0067-0049/181/2/391)
- Tremblay, G. R., Combes, F., Oonk, J. B. R., et al. 2018, *ApJ*, 865, 13, doi: [10.3847/1538-4357/aad6dd](https://doi.org/10.3847/1538-4357/aad6dd)
- Trott, C. R., Lebrun-Grandié, D., Arndt, D., et al. 2022, *IEEE Transactions on Parallel and Distributed Systems*, 33, 805, doi: [10.1109/TPDS.2021.3097283](https://doi.org/10.1109/TPDS.2021.3097283)
- Turk, M. J., Smith, B. D., Oishi, J. S., et al. 2011, *The Astrophysical Journal Supplement Series*, 192, 9, doi: [10.1088/0067-0049/192/1/9](https://doi.org/10.1088/0067-0049/192/1/9)
- . 2024, *Introducing yt 4.0: Analysis and Visualization of Volumetric Data*, <https://yt-project.github.io/yt-4.0-paper/>
- Vantyghem, A. N., McNamara, B. R., Russell, H. R., et al. 2014, *MNRAS*, 442, 3192, doi: [10.1093/mnras/stu1030](https://doi.org/10.1093/mnras/stu1030)
- Vantyghem, A. N., McNamara, B. R., O’Dea, C. P., et al. 2021, *ApJ*, 910, 53, doi: [10.3847/1538-4357/abe306](https://doi.org/10.3847/1538-4357/abe306)
- Voit, G. M., Cavagnolo, K. W., Donahue, M., et al. 2008, *ApJL*, 681, L5, doi: [10.1086/590344](https://doi.org/10.1086/590344)
- Voit, G. M., Meece, G., Li, Y., et al. 2017, *ApJ*, 845, 80, doi: [10.3847/1538-4357/aa7d04](https://doi.org/10.3847/1538-4357/aa7d04)
- Voit, G. M., Bryan, G. L., Prasad, D., et al. 2020, *ApJ*, 899, 70, doi: [10.3847/1538-4357/aba42e](https://doi.org/10.3847/1538-4357/aba42e)
- Wang, C., Ruszkowski, M., Pfrommer, C., Oh, S. P., & Yang, H.-Y. K. 2021, *Monthly Notices of the Royal Astronomical Society*, 504, 898–909, doi: [10.1093/mnras/stab966](https://doi.org/10.1093/mnras/stab966)
- Weinberger, R., Su, K.-Y., Ehlert, K., et al. 2023, *MNRAS*, 523, 1104, doi: [10.1093/mnras/stad1396](https://doi.org/10.1093/mnras/stad1396)
- Wibking, B. D., Voit, G. M., & O’Shea, B. W. 2024, *arXiv e-prints*, arXiv:2410.03886, doi: [10.48550/arXiv.2410.03886](https://doi.org/10.48550/arXiv.2410.03886)
- Yang, H. Y. K., & Reynolds, C. S. 2016, *ApJ*, 818, 181, doi: [10.3847/0004-637X/818/2/181](https://doi.org/10.3847/0004-637X/818/2/181)
- Zhou, M., Zhdankin, V., Kunz, M. W., Loureiro, N. F., & Uzdensky, D. A. 2024, *ApJ*, 960, 12, doi: [10.3847/1538-4357/ad0b0f](https://doi.org/10.3847/1538-4357/ad0b0f)
- ZuHone, J. A., Kunz, M. W., Markevitch, M., Stone, J. M., & Biffi, V. 2015, *ApJ*, 798, 90, doi: [10.1088/0004-637X/798/2/90](https://doi.org/10.1088/0004-637X/798/2/90)